

Aerosols in the Energy Exascale Earth System Model (E3SM) version 1: New developments and their impacts on radiative forcing

Hailong Wang^{1*}, Richard Easter¹, Rudong Zhang¹, Po-Lun Ma¹, Balwinder Singh¹, Kai Zhang¹, Dilip Ganguly^{1,2}, Philip Rasch¹, Susannah Burrows¹, Steve Ghan¹, Sijia Lou¹, Yun Qian¹, Yang Yang^{1,3}, Yan Feng⁴, Mark Flanner⁵, Ruby Leung¹, Xiaohong Liu^{6,9}, Manish Shrivastava¹, Jian Sun¹, Qi Tang⁷, Shaocheng Xie⁷, Jin-Ho Yoon^{1,8}

¹Pacific Northwest National Laboratory, Richland, WA

²Indian Institute of Technology (IIT) Delhi, Hauz Khas, New Delhi, India.

³Nanjing University of Information Science and Technology, Nanjing, Jiangsu, China

⁴Argonne National Laboratory, Lemont, IL

⁵University of Michigan, Ann Arbor, MI

⁶University of Wyoming, Laramie, WY

⁷Lawrence Livermore National Laboratory, Livermore, CA

⁸Gwangju Institute of Science and Technology, Gwangju, South Korea

⁹now at Texas A&M University, College Station, TX

*Correspondence to: Hailong.Wang@pnnl.gov

Key points:

1. A description and assessment of new aerosol treatments in the Energy Exascale Earth System Model version 1 (E3SMv1) is provided
2. Contributions to the total aerosol-related radiative forcing by individual new treatments and different processes are quantified
3. Some of the new treatments are found to depend on model physics and require further improvement for E3SM or other Earth system models

This article has been accepted for publication and undergone full peer review but has not been through the copyediting, typesetting, pagination and proofreading process which may lead to differences between this version and the Version of Record. Please cite this article as doi: 10.1029/2019MS001851

Abstract

The new Energy Exascale Earth System Model version 1 (E3SMv1) developed for the U.S. Department of Energy has significant new treatments of aerosols and light-absorbing snow impurities as well as their interactions with clouds and radiation. This study describes seven sets of new aerosol-related treatments (involving emissions, new particle formation, aerosol transport, wet scavenging and resuspension, and snow radiative transfer) and examines how they affect global aerosols and radiative forcing in E3SMv1. Altogether they give a reduced total aerosol radiative forcing (-1.6 W m^{-2}) and sensitivity in cloud liquid water to aerosols, but an increased sensitivity in cloud droplet size to aerosols. A new approach for H_2SO_4 production and loss largely reduces a low bias in small particles concentrations and leads to substantial increases in CCN concentrations and cloud radiative cooling. Emitting secondary organic aerosol (SOA) precursor gases from elevated sources increases the column burden of SOA, contributing substantially to global clear-sky aerosol radiative cooling (-0.15 out of -0.5 W m^{-2}). A new treatment of aerosol resuspension from evaporating precipitation, developed to remedy two shortcomings of the original treatment, produces a modest reduction in aerosols and cloud droplets; its impact depends strongly on the model physics and is much stronger in E3SM version 0. New treatments of the mixing state and optical properties of snow impurities and snow grains introduce a positive present-day shortwave radiative forcing (0.26 W m^{-2}), but changes in aerosol transport and wet removal processes also affect the concentration and radiative forcing of light-absorbing impurities in snow/ice.

Plain Language Summary

Aerosol and aerosol-cloud interactions continue to be a major uncertainty in Earth system models, impeding their ability to reproduce the observed historical warming and to project changes in global climate and water cycle. The U.S. DOE Energy Exascale Earth System Model version 1 (E3SMv1), a state-of-the-science Earth system model, was developed to use exascale computing to address the grand challenge of actionable predictions of variability and change in the Earth system critical to the energy sector. It has been publicly released with new treatments in many aspects, including substantial modifications to the physical treatments of aerosols in the atmosphere and light-absorbing impurities in snow/ice, aimed at reducing some known biases or correcting model deficiencies in representing aerosols, their life cycle, and their impacts in various components of the Earth system. Compared to its predecessors (without the new treatments) and observations, E3SMv1 shows improvements in characterizing global distributions of aerosols and their radiative effects. We conduct sensitivity experiments to understand the impact of individual changes and provide guidance for future development of E3SM and other Earth system models.

1. Introduction

Aerosols play many important roles in Earth's climate with cascading microphysical, radiative, and dynamical effects (Boucher et al., 2013), in addition to their impact on air quality and atmospheric visibility (e.g., Yang et al., 2018a). They can directly modify Earth's energy budget by scattering and/or absorbing solar and terrestrial radiation. Certain types of aerosols can act as nuclei for cloud droplet and/or ice crystal formation, leading to their effects on clouds and precipitation, which in turn can impact the removal of aerosols from the atmosphere, the energy budget, and many other aspects of the Earth system. When light-absorbing aerosols deposit on snow or ice surfaces, they may speed up the melting through the additional absorption of solar radiation (e.g., Warren and Wiscombe, 1980; Flanner et al., 2007; Qian et al., 2011, 2015), which has additional important implications for climate change and seasonal distribution of water resource (e.g., Rahimi et al., 2019). The understanding of detailed physical and chemical processes for aerosols and their interactions with other components of the climate system has been obtained from laboratory experiments, field observations, or process modeling studies (e.g., Shilling et al., 2009; Wang et al., 2011; Carslaw et al., 2013; Rosenfeld et al., 2014; Srivastava et al., 2015; Fanourgakis et al., 2019; Sorooshian et al., 2019). They are very challenging to treat accurately in Earth system models (ESMs) that are relied upon to represent and understand the complex global impact of aerosols and their interactions with the coupled aerosol-cloud-radiation-dynamics system (e.g., Mann et al., 2014; Gettelman 2015; Zhang et al., 2016; Ghan et al., 2016; Gryspenrdt et al. 2017). The latest report by the Intergovernmental Panel on Climate Change (IPCC, 2013) identified aerosol-cloud interactions as the largest source of uncertainty in estimating historical anthropogenic radiative forcing, which is critical for climate models to reproduce the observed trends in global warming.

Much of the large uncertainty and diversity of CMIP5 (Coupled Model Intercomparison Project Phase 5) models in aerosol radiative forcing comes from crude model treatments of aerosols and their effects. Some of the CMIP5 models, including the Community Earth System Model (CESM), did not yet consider the impact of aerosols on cloud microphysical processes in convective and ice clouds. Aerosol indirect forcing was found to be fairly sensitive to aerosol and cloud microphysical treatments within the same model (e.g., CESM) and between different models (e.g., Zhang et al., 2016; Ghan et al., 2016). The representation of aerosols, their lifecycle and effects in the coupled system (particularly, emissions, particle formation/growth, transport, droplet nucleation, wet scavenging and removal processes) still relies on parameterization schemes that use a variety of assumptions to relate subgrid-scale quantities to grid-scale variables. With the rapid increase in computing power, Earth system modeling has aimed at increasing model resolution, although it hasn't reached global convection-permitting resolution yet. Nevertheless, the increasing computational power allows for more comprehensive and sophisticated schemes to be considered in aerosol-climate modeling to reduce known biases and advance scientific understanding.

The U.S. DOE Energy Exascale Earth System Model (E3SM) version 1 was developed from the Community Earth System Model (CESM1.3) but has evolved with significant new developments in all individual components, including totally new ocean and sea-ice components based on the Model for Prediction Across Scales (MPAS) framework and a new river model (i.e., Model for Scale Adaptive River Transport (MOSART)) (Golaz et al. 2019). The atmospheric component of E3SMv1 (a.k.a. EAMv1), based on the Community Atmosphere Model version 5.3 (CAM5.3, also referred to as EAMv0), has substantial modifications to the physical treatments of aerosols, clouds, and cloud-aerosol interactions

along with several other innovations in atmospheric physics (Rasch et al., 2019; Xie et al., 2018).

Compared to EAMv0, the EAMv1 was designed to run at a low horizontal resolution of 1° (30 spectral elements) and a high horizontal resolution of 0.25° (120 spectral elements) for different scientific applications. Both configurations have 72 layers (compared to 30 layers in EAMv0) in the vertical for dynamics and physics, with 14 layers below 850 hPa and the model top at 0.1 hPa. New physics parameterizations in EAMv1 include the Cloud Layers Unified By Binormals (CLUBB) parameterization for shallow convection, turbulent transport, and cloud macrophysics (Golaz et al., 2002; Larson et al., 2002; Bogenschutz et al., 2013), an updated cloud microphysics scheme with a fully prognostic treatment of rain and snow (Gettelman and Morrison, 2015), new treatments of convective transport, wet removal, and resuspension of aerosols (Wang et al., 2013; Liu et al., 2016), and updated mixed-phase cloud ice microphysics (e.g., Wang et al., 2014). EAMv1 uses four internally mixed log-normal size modes (MAM4) to represent the size distribution and mixing state of aerosols (Liu et al., 2016) with several enhanced features as detailed in Section 2.

There were some known deficiencies in the representation of aerosols and/or aerosol-cloud interactions in CAM5.3 and EAMv0. Precipitation scavenging is generally the primary removal mechanism for tropospheric submicron aerosol particles, and is also important for coarse aerosol particle removal. Extensive research on precipitation scavenging has been done over the last 50+ years. In contrast, the resuspension of aerosol material from evaporating precipitation has received very little attention. The original treatments of aerosol precipitation scavenging and resuspension from evaporating precipitation for MAM4 in CAM5.3 (and earlier CAM5 versions) are based on the treatments used in the bulk aerosol model (developed for CAM version 3). As a result, the MAM4 treatments contained two assumptions that were not critically evaluated at the time. One assumption is that aerosol

material resuspended from evaporating precipitation is returned to the originating aerosol mode (i.e., scavenged accumulation-mode sulfate is returned to the accumulation mode). The other assumption is that the resuspended aerosol mass is proportional to the water mass of partially evaporated raindrops. In reality, raindrops typically form from hundreds to thousands of cloud droplets (as indicated by their typical sizes and number concentrations), so each raindrop contains the aerosol material from many scavenged aerosol particles that acted as cloud condensation nuclei (CCN), and the resuspended aerosol particles from completely evaporated raindrops are mostly in the coarse-particle size range (e.g., Mitra et al., 1992).

There is also a notable bias in CAM5 simulated concentrations of small particles. According to the model intercomparison study by Mann et al. (2014), CAM5 underestimates background small particles (dry diameter < 100 nm) that can grow and serve as sources of potential CCN. Such bias likely still exists in EAMv0. The concentration of small particles, especially ultrafine particles, is largely determined by new particle formation and gas-to-particle conversion, involving precursor SO₂ and organic gases. We aim to improve the model representation of relevant processes in EAMv1.

Many ESMs, including CESM and E3SMv0, consider the deposition of light absorbing particles (e.g., BC and dust) and their impact on surface snow and ice. Through darkening the bright snow surface, BC and dust impurities have been shown to account for a large portion of the total light absorption at visible wavelengths by surface snow near heavily polluted regions such as East Asia (e.g., Zhang et al., 2013; Dang et al., 2017). Although the global mean radiative forcing of BC in snow and sea ice (best estimate) is about +0.04 W m⁻² (Bond et al., 2013; IPCC, 2013), depending on the location and season, the regional radiative forcing perturbation (with and without the presence of BC in snow) can be as high as 25 W m⁻² at lower latitudes during spring and summer (e.g., Flanner et al., 2007; Kopacz et al.,

2011; Qian et al., 2011, 2015; Zhang et al., 2015; Wu et al., 2018). Physically accurate treatments of surface deposition of BC/dust particles and radiative transfer in snow and ice are important for models to represent particle impacts on snow/ice albedo and surface energy balance. There are many assumptions employed in ESMs that cause biases in the representation of the impact of snow/ice impurities (e.g., Qian et al., 2014), of which E3SMv1 has some intended improvements compared to E3SMv0.

All the improvements made in treating aerosols, aerosol-cloud interactions and light-absorbing particles in snow/ice are aimed at reducing model deficiencies and biases in emissions, new particle formation, aerosol transport, radiative transfer calculation, wet scavenging and/or resuspension processes, as mentioned above. In this study we summarize the new aerosol treatments and describe how they affect aerosols and radiative forcing in E3SMv1, both individually and collectively.

The paper is organized as follows. Section 2 describes aerosol representation and new treatments for aerosols implemented in E3SMv1. Section 3 summarizes model experiments conducted to quantify the impact of some individual modifications on the global distribution of aerosols and aerosol forcing estimation. The results, including model evaluation and comparison to old model treatments, are then shown in Section 4, with an emphasis on the new treatments that are not published elsewhere. Section 5 provides a brief summary of key conclusions.

2. Description of new developments for aerosols and light absorbing particles in E3SMv1

2.1 Aerosol representation

Like the other model components, the representation of atmospheric aerosols and their roles in the Earth system by EAMv1 was inherited from the global aerosol-climate model EAMv0 and its modal aerosol module (MAM). It treats a combination of processes, as illustrated in

Fig. 1, controlling the evolution of aerosols that are either directly emitted or converted from precursor gases from a variety of natural and anthropogenic sources. The processes include transport (by grid-scale wind, sub-grid turbulence, convection, and sedimentation), aerosol microphysics (i.e., particle nucleation, condensation/evaporation of trace gases, aging, and coagulation), cloud processing (i.e., aqueous chemistry, scavenging by hydrometeors, resuspension from evaporating hydrometeors, and wet deposition), and dry deposition.

Aerosol species in MAM of EAMv0 include sulfate, primary organic aerosol (POA), secondary organic aerosol (SOA), black carbon (BC), sea salt, and mineral dust. Brown carbon and nitrate aerosols are currently not treated in CESM and E3SM but are planned for future generations of E3SM. The size distribution and mixing-state of aerosol particles are represented by MAM using three, four, or seven log-normal size modes (called MAM3, MAM4 and MAM7, respectively), as described by Liu et al. (2012, 2016). Figure 2 depicts the four size modes and aerosol species therein for MAM4 in EAMv0 and new additions (underlined species) for the further developed MAM4 in EAMv1 that are described in more detail below. All aerosol species within each of the four individual modes is assumed to be internally mixed and represented by a single number concentration, while particles are externally mixed among the different modes. One important difference between MAM3 and MAM4/MAM7 is that the freshly emitted primary carbonaceous aerosols (e.g., BC and POA) are immediately mixed with highly hygroscopic species and subject to wet scavenging and removal in MAM3 while MAM4/MAM7 has an additional primary-carbon mode to treat the aging process of BC/POA. MAM4 is selected for EAMv1 for its explicit treatment of the aging process, during which the condensation of H_2SO_4 and organic gases forms mono-layers of hygroscopic coating on fresh BC/POA particles or coagulation with Aitken mode particles adds soluble mass, making them viable CCN, but it still has a better computational efficiency than MAM7.

Aerosol particles in CESM and E3SM are either suspended in the clear air (i.e., interstitial attachment state) or embedded in cloud droplets (i.e., cloud-borne state) or precipitation particles (i.e., precipitation-borne state). The interstitial and cloud-borne aerosol particles are treated explicitly as tracer species in the model, while precipitation-borne aerosol is only treated in the wet-removal section of the model. Hygroscopic interstitial particles within the cloudy portion of a grid cell are activated to the cloud-borne state through droplet nucleation, which is parameterized using supersaturation determined by grid-scale and sub-grid vertical velocity and aerosol properties following Abdul-Razzak and Ghan (2000). Aerosol particles in both interstitial and cloud-borne states are subject to dry and wet deposition (removal) in the model. Dry deposition is parameterized using the approach of Zhang et al. (2001), which considers particle sizes, friction velocity, aerodynamic resistance, and surface properties provided by the land model.

For the aerosol wet removal, the model considers in-cloud and below-cloud scavenging processes (e.g., Wang et al., 2013). Below-cloud scavenging refers to the capture of interstitial aerosol by precipitation particles through Brownian diffusion or inertial impaction. In-cloud scavenging refers to the transfer of cloud-borne aerosol to precipitation-borne through cloud processes that convert/transfer cloud droplets to precipitation. When cloud droplets (or raindrops) evaporate, a portion of cloud-borne (or precipitation-borne) aerosol is returned to the interstitial state via the resuspension process, and the resuspension treatment in the model has an impact on aerosol redistributions and on clouds and precipitation. As described below, the treatment of resuspension of aerosol particles from evaporated raindrops is modified in EAMv1 along with several other improvements to the representations of aerosols and cloud-aerosol interactions as well as deposition of light-absorbing particles (e.g., dust and BC) to snowpack and ice.

The new treatments of aerosols in E3SMv1 that are illustrated in the schematic diagram of Fig. 1 are described in more detail below.

2.2 Improved treatment of H₂SO₄ vapor for new particle formation

H₂SO₄ vapor strongly affects new particle formation, and because of its short lifetime (due to condensation onto existing aerosol particles) it is sensitive to the time splitting. In order to improve the simulated concentrations of smaller aerosol particles (diameter $D_p < 100$ nm), the treatments of H₂SO₄ vapor production (by SO₂ gas-phase oxidation) and loss (by condensation onto particles) have been modified to use a parallel time-splitting approach, rather than the serial time-splitting approach in E3SMv0. The parallel time-splitting approach is similar to that described in Kokkola et al. (2009) and Wan et al. (2013), but the aerosol nucleation process is still calculated in a separate step, following the production and condensation. This approach provides H₂SO₄ vapor concentrations to the aerosol nucleation (new particle formation) process that are numerically more accurate compared to the E3SMv0 approach (Wan et al., 2013). Simulated aerosol number concentrations are expected to increase, particularly, for small particles ($D_p < 100$ nm) in the Aitken model. This is evaluated against surface observations (in the Section 4).

2.3 Improved SOA treatment

The standard CAM5.3 and E3SMv0 use a highly simplified lumped-species SOA treatment that has a single SOA aerosol species in selected modes and a single condensable organic gas species (referred to as SOAG). The SOAG species is emitted at the surface, and its emissions were obtained by applying estimated SOA yields to emissions of five primary Volatile Organic Compound (VOC) gas species treated in the MOZART gas-chemistry mechanism (Emmons et al., 2010): isoprene, lumped terpenes, lumped aromatics, and higher molecular-weight lumped alkanes and alkenes. An additional factor of 1.5 was applied to the SOAG emissions to increase simulated SOA concentrations to better match the observed present-day

organic aerosol loading (e.g., Liu et al., 2012). Moreover, the assumed volatility of SOAG is relatively low (i.e., saturation vapor concentration is 7.1×10^{-11} kg m⁻³ at 288 K and 1 atm), so it condenses fairly rapidly near the surface where it is emitted, without considering any chemical aging that converts higher volatility condensable organic gases to lower volatility ones.

In the new treatment of SOA in E3SMv1, the SOAG source (i.e., emissions) is derived from the FragNVSOA simulation of Shrivastava et al. (2015, hereafter S2015) by scaling its condensation sources to the appropriate primary precursor emissions. The S2015 FragNVSOA used an explicit treatment of multigenerational SOA precursor-gas chemistry, with both functionalization and fragmentation (Frag) reactions, and particle-phase oligomerization that transforms SOA to effectively non-volatile (NVSOA). This treatment was computationally expensive but produced three-dimensional spatial distributions of organic aerosols in better agreement with existing measurements. The SOAG source for E3SMv1 is taken as the overall SOA condensation rate in the S2015 simulation, derived from monthly model history files, and the source is throughout the atmosphere rather than just at the surface. S2015 had three source-tagged categories of SOA gas and aerosol species, each with a range of volatilities: biomass burning plus biofuel use (BB), fossil fuel use (FF), and biogenic (BG). The SOA condensation rate from the BB category was scaled by 0.25 because modeled aerosol optical depths over equatorial Africa and the adjacent Atlantic Ocean were much too high. Using this prescribed SOAG source with the single lumped SOAG species improves the simulated SOA distributions while significantly reducing the computational cost of advecting multiple gas- and particle-phase SOA species in S2015. Future versions of E3SM will include online SOA chemistry calculations rather than deriving SOAG emissions from the previous treatment of S2015.

2.4 New MOA species

A new representation of primary marine organic aerosol (MOA), based on the OCEANFILMS parameterization for emissions in sea spray aerosol (Burrows et al., 2014), has been implemented in EAMv1. This MOA treatment represents an important step towards linking ocean biogeochemistry process models to the sea surface chemistry that determines sea spray aerosol formation. The organic mass fraction of sea spray aerosol calculated according to Burrows et al (2014) is applied directly to Aitken mode, primary-carbon mode and/or accumulation mode within MAM4, depending on the assumption of its mixing with sea salt. For the fully internal mixture assumption, MOA is emitted to both Aitken and accumulation modes along with sea salt; otherwise, MOA is emitted to the primary-carbon mode only, like POA. The MOA emitted mass flux can be treated by assuming that (1) the experimentally-derived sea-spray aerosol emitted mass flux parameterization represents the sum of organics and inorganics, so that the MOA mass emissions *reduce* the inorganic sea-salt emissions, or (2) the emissions parameterization only accounts for inorganic sea salt, so that the MOA mass emissions are *added* onto the inorganic emissions. As shown in sensitivity tests and comparison to experimental evidence by Burrows et al. (2018), the INT_ADD case (i.e., organic emissions internal mixed and added) is identified to be the most physically-realistic configuration and thus selected as the default for EAMv1.

The impact of MOA on global aerosols and clouds have been extensively evaluated by Burrows et al. (2018) in the EAMv0 framework. They found that cloud droplet number and liquid water path have a substantial increase in response to the new MOA treatment (by adding organic mass to the original sea salt emissions), leading to an additional cloud shortwave cooling with a global annual mean of -0.36 W m^{-2} and regional mean of -1.6 W m^{-2} over the Southern Ocean in austral summer (DJF).

2.5 Improvements to the convective transport of aerosols and their wet removal

Like many other global aerosol-climate models, EAMv0 (CAM5.3) has large biases in the estimate of aerosol concentrations in distant regions from major sources due to model deficiencies in the representation of aerosol transport and removal (e.g., Wang et al., 2013; Liu et al., 2012, 2016). Aiming at improving model simulations of aerosol spatial distributions (especially for the upper troposphere and high latitudes), Wang et al. (2013) introduced into CAM5 a suite of modified treatments of aerosol transport and wet removal that included (1) an improved treatment of aerosol scavenging by stratiform liquid clouds and (2) a new unified treatment of aerosol vertical transport and wet removal by convective clouds with secondary activation for aerosols above cloud base (e.g., mostly for particles laterally entrained into convective updrafts). The new treatments were found to improve global aerosol distributions that further affect cloud and climate simulations (Wang et al., 2013). These modifications, which were not fully adapted in CAM5.3, are included in the EAMv1.

2.6 Improvements to aerosol-affected cloud microphysical processes

EAMv1 uses the two-moment bulk microphysics for stratiform clouds with prognostic rain (Gettelman et al., 2015), which is also connected to the shallow cumulus and turbulence parameterization CLUBB to allow interactions of aerosols with shallow convective clouds as well (Xie et al., 2018; Rasch et al., 2019). The cloud-to-rain conversion rate in EAMv0, based on an autoconversion parameterization originally developed by Khairoutdinov and Kogan (2000) was found to have an overly strong dependency on the cloud-droplet number concentration (e.g., Wang et al., 2012). Adjusting three tunable parameters in the autoconversion formulation, using similar relationships derived from observations, reduces this dependency and also leads to a more reasonable aerosol second indirect effect. In addition, several changes related to ice microphysics are made to EAMv1. The heterogeneous ice formation in mixed-phase clouds, based on the classical nucleation theory and linked to

both interstitial and cloud-borne dust and black carbon aerosols (Wang et al., 2014), is adopted in EAMv1. Like the cloud-to-rain conversion process, the ice-to-snow conversion is also quite important to cloud forcing but very uncertain in EAMv0. The threshold size at which growing ice crystals are converted to snow particles, which is a constant-valued tunable parameter in EAMv0, is replaced with an empirical formulation that treats the size as a function of temperature in EAMv1.

2.7 New treatments of aerosol resuspension from evaporating precipitation

Precipitation scavenging (i.e., wet removal) has long been recognized as one of the major removal processes for tropospheric aerosol particles and the dominant one for accumulation-mode size particles. A significant fraction of the aerosol material that is wet-scavenged within clouds can be resuspended when raindrops evaporate below cloud, and this resuspension has received much less attention than the scavenging process. When cloud droplets evaporate, the aerosol material in each drop is often primarily from the CCN on which the droplet originally formed, so the resuspended aerosol particles are similar in size to the original CCN. In contrast, each raindrop generally collects thousands of cloud droplets and the aerosol material within them, as indicated by the very different number concentrations and sizes of rain drops vs. cloud droplets. When a raindrop completely evaporates, its aerosol material is resuspended as a single particle that is generally in the coarse (i.e., super-micron) aerosol-particle size range (e.g., Mitra et al., 1992). The original MAM treatment of aerosol resuspension from evaporating precipitation (which is in CAM5.3 and EAMv0) puts aerosols back to their originating mode rather than to the coarse mode. This shortcoming resulted from attempting to minimize changes to CAM's existing aerosol wet-removal code (designed for bulk aerosols) when MAM was first implemented. A second but less serious shortcoming of the original MAM treatment is its assumption that the precipitation-borne aerosol resuspension is directly proportional to the precipitation water evaporation. According to

Mitra et al. (1992), when rain partially evaporates, the smaller drops evaporate completely and resuspend all of their aerosol material, but the larger drops evaporate partially and resuspend no aerosol material, so the aerosol resuspension percentage will be less than the water evaporation percentage.

A new treatment of aerosol resuspension from evaporating precipitation has been developed that eliminates these two shortcomings. In the new treatment in EAMv1, the resuspended aerosol material is placed in the coarse mode, with particle size determined by the amount of resuspended aerosol mass and the number of completely evaporated raindrops, both of which are provided by a new parameterization of raindrop size spectrum evolution during below-cloud evaporation (Appendix A). This parameterization is based on a simple drop-size resolved model of rain evaporation as it falls through sub-saturated air, which provides the resuspended aerosol mass and number amounts as non-linear functions of the precipitation water evaporation (shown in Figures A1 and A2). More detailed technical aspects regarding how aerosol mass and number resuspension are treated for stratiform and convective precipitation in E3SMv1 are described in Appendix B.

2.8 Integration of MAM4 with new treatments of light-absorbing particles in snow/ice

All changes made to atmospheric aerosols that affect dry and wet deposition of light-absorbing particles (i.e., BC and dust) are also linked to the impact of these particles on snow and ice. The E3SMv1 has also been modified to improve the compatibility between MAM4 and treatment of light-absorbing particles deposited on snow/ice to better simulate their impacts on snow/ice melting and the surface energy budget. In particular, the new scheme treats both external mixing and internal mixing (within-hydrometeor) of BC and snow grains (Flanner et al., 2012) rather than only external mixing in E3SMv0. The within-hydrometeor mixing treatment is expected to increase in-snow BC radiative forcing, as BC particles encased in ice grains absorb more solar radiation per unit mass of BC (Flanner et al., 2012).

The atmospheric aerosol deposition code is modified to separately treat the deposition of atmospheric BC mixed internally within hydrometeors and externally to hydrometeors, and to partition dust into four size bins instead of two. In E3SMv1, the original Snow, Ice and Aerosol Radiative (SNICAR) model (Flanner et al., 2007) is modified to take size-dependent BC optical properties (i.e., depending on both snow grain size and BC particle size) and provide a new lookup table for the optical properties accordingly. Similar modifications are done to the sea ice component to take new size-dependent BC optical properties, in which the radiative transfer calculation is different from SNICAR. However, the radiative transfer calculation has been unified for terrestrial snow, sea ice, and snow atop sea ice (Dang et al., 2019) that is planned for use in future versions of E3SM (rather than the E3SMv1). Finally, the code has been structured to function with future treatments of light-absorption by brown carbon (as part of the deposited POA and SOA) particles in addition to black carbon and dust.

3. Model experiments for sensitivity tests and aerosol forcing estimation

Two sets of experiments are conducted and analyzed to assess aerosols and aerosol radiative forcing as well as the impact of some individual modifications on the global distribution of aerosols and their radiative forcing in EAMv1 (30 spectral elements or 1°). Unless specified, all the simulations are performed using EAMv1.

- 1) Two-year (2006-2007) simulations (summarized in Table 1) with winds nudged to reanalysis (Zhang et al., 2014) to compare with observations and the AeroCom Indirect Effects experiments (Ghan et al., 2016). Two simulations with pre-industrial (PI) and present-day (PD) aerosol emissions, respectively, are conducted for each sensitivity test (i.e., with all new treatments included or an individual new treatment excluded). The difference between the two gives the conventional estimate of total aerosol forcings, while the difference between each of the sensitivity experiment (with

one new treatment excluded) and the control experiment (CTRL) is used to assess the impact of the individual new treatment in the EAMv1 framework.

- 2) A two-year (2006-2007) simulation with winds nudged to the same reanalysis as in PD CTRL but without the new treatments of light-absorbing particles in snow and sea ice for (noNewInSnow in Table 1).
- 3) A two-year (2006-2007) simulation same as PD CTRL but with the linearized version of the new resuspension treatment, in which both the fraction of aerosol material resuspended and the fraction of raindrops that fully evaporate are assumed equal to the fraction of precipitation mass-flux that evaporates (see Appendix A).
- 4) A set of three 11-year free-running EAMv0 simulations with the old resuspension, new-linear resuspension, and new-nonlinear resuspension treatment, respectively, under present-day conditions (including CMIP5 aerosols).
- 5) A 15-year (2000-2014) AMIP-type free-running simulation (CTRL15) that was originally conducted by Golaz et al. (2019) is used here to compare with the PD short simulation (CTRL) for aerosol spatial distribution in EAMv1.

In all EAMv1 simulations, emissions of anthropogenic and biomass burning aerosols are from CMIP6 data sets, except that SOAG emissions are derived from SOA formation rates from a S2015 simulation to improve the SOA representation in the model, as described in Section 2.3. Instead of using yearly varying aerosol emissions for 2006-2007, we use the average between 2000-2014 to represent present-day aerosol conditions by removing the interannual variation in emissions (Yang et al., 2018a, b) and in aerosol forcing estimates (e.g., Golaz et al., 2019). Pre-industrial emissions use the CMIP6 data set for year 1850. The Modern Era Retrospective-Analysis for Research and Applications, Version 2 (MERRA-2; Gelaro et al., 2017) reanalysis is used to constrain the model wind fields with a relaxation timescale of 6 hours in the nudged simulations. The same nudging methodology has been

used in previous AeroCom model intercomparison studies for aerosol indirect effects among different climate models or within the same model with modified aerosol-cloud physics (e.g., Ghan et al., 2016; Gryspeerd et al. 2017). Sun et al. (2019) found that the interannual variability of mean present-day cloud forcing in EAMv1 is small for the nudged-wind simulations.

4. Results and Discussions

4.1 Validation and sensitivity analysis of new aerosol treatments

Some of the individual new treatments have been validated and evaluated in previous studies within the EAMv0 or EAMv1 framework (Wang et al., 2013; Wang et al., 2014; Liu et al., 2016; Burrows et al., 2018). In this study we mainly focus on three of the new features: the treatment of aerosol resuspension from rain evaporation (NewResusp), the treatment of SOA formation, and the time-splitting approach for H₂SO₄ vapor production/loss (NewH2SO4). Among these three, the NewResusp treatment has been tested in both EAMv1 and EAMv0, and detailed process-level analysis is presented here because we found a strong sensitivity of its impact on aerosols and CCN to the model representation of cloud microphysics. The detailed analysis is likely to be useful for other climate models to consider this new treatment as well.

4.1.1 Sensitivity to the resuspension treatment

4.1.1.1 Global average aerosol and cloud parameters

Table 2 shows the global, annual averages of aerosol mass burdens, aerosol optical depth (AOD) and absorption AOD, and several aerosol number, cloud microphysical, and cloud radiative parameters for the EAMv1 (hereafter V1) and EAMv0 (hereafter V0) simulations with the new-nonlinear, new-linear, and old resuspension treatments (see Appendix A). For the new-linear and old resuspension treatment simulations, results are given as percentage differences from the corresponding (V0 or V1) new-nonlinear simulation. For V1, the old

resuspension mass burdens and AOD are 3-9% greater than the new-nonlinear resuspension values. For species like sulfate, BC, POA, and SOA that are predominantly in the accumulation and primary-carbon modes, this is due to the resuspended mass having a shorter lifetime when it goes into the coarse mode. For example, lifetimes of accumulation and coarse-mode species (for V1 old treatment) are 6.18 and 3.46 d for sulfate, 7.31 and 1.84 d for mineral dust, and 1.70 and 0.60 d for sea salt. For mineral dust and sea salt which are predominantly (over 88%) in the coarse mode regardless of the resuspension treatment, the burden differences are primarily due to the somewhat larger coarse-mode particle sizes with the new-nonlinear resuspension treatment, which increases the coarse-mode dry-deposition and below-cloud wet-removal rates compared to the old resuspension treatment. The non-linear resuspension also contributes to the burden differences. Burden and AOD differences between the old and new-nonlinear treatment are much larger in the V0 simulations (14-33%). The much greater sensitivity to the resuspension treatment in V0 is primarily due to stronger evaporation of stratiform precipitation in V0, which is discussed later in this section.

Differences between the old and new-linear resuspension treatments for mode number concentrations, CCN (at 0.1% supersaturation), and cloud droplet number in the V1 simulations are modest. Differences are again much larger in the V0 simulations. Accumulation and primary-carbon mode number are 18% and 11% higher with the old resuspension, while Aitken mode number is 19% lower. The primary-carbon mode difference is caused by slower aging rather than resuspension of particles in this mode; and the Aitken mode difference is primarily caused by lower formation by nucleation, because of more rapid H₂SO₄ condensation onto pre-existing particles. The CCN concentrations in the lower and entire troposphere are 36-38% higher. These CCN are mostly accumulation mode particles with dry-diameters ≥ 100 nm. The large difference is due both to more accumulation-mode particles and larger sizes in the old resuspension simulation. The higher

CCN concentrations lead to 36% higher cloud-droplet number concentrations and somewhat higher cloud liquid water (11%).

Differences between the new-linear and new-nonlinear resuspension treatment simulations are much smaller than the differences between the old and new-nonlinear treatments. Mass burdens are 1-3% greater with new-linear in V1 and 3-7% greater in V0. The mode number concentrations, CCN, and CDNC differences between new-linear and new-nonlinear are 1% or less in both V1 and V0. These results indicate that the nonlinear aspect of the new treatment has much less impact than the resuspension to coarse mode aspect, and thus the new-linear treatment (which is simpler to implement) is a reasonable approach at least in the global mean.

4.1.1.2 Precipitation production and evaporation

To better understand these results, particularly the differences between the V1 and V0 results, it is useful to look at the precipitation evaporation that drives the resuspension. Table 3 presents the global, annual averages of precipitation production, surface precipitation, and evaporated fraction from the stratiform, shallow convective, and deep convective clouds in the V0 and V1 models. Note that the V1 model with CLUBB does not have separate treatments of stratiform and shallow convective clouds. These results are from the new-nonlinear resuspension simulations but differ very little in the other sensitivity simulations.

Total precipitation is similar for V0 and V1, with the higher V1 values partially due to that simulation being nudged, and deep convection accounts for 59% of the total precipitation in both. The most notable results are that the stratiform evaporation is much higher in the V0 simulation than V1, and the stratiform (or stratiform and shallow convection) evaporation fractions are much higher than that of the deep convective in both models. The V0/V1 stratiform evaporation differences are likely due to the use of Morrison and Gettelman (2008; hereafter MG) microphysics in V0 versus Gettelman and Morrison (2015; hereafter MG2)

microphysics in V1 (e.g., diagnostic vs. fully prognostic treatments of rain and snow in MG vs. MG2, respectively), although other V0/V1 differences (model physics, vertical and horizontal resolution) may contribute. Simulations for a different study (work in progress) with the CAM5.5 model that used MG2 microphysics and had resolutions similar to V0 here also had much lower stratiform precipitation evaporation compared to V0. The lower stratiform evaporation in V1 reduces the importance of the aerosol resuspension from evaporation, as well as the sensitivity to the NewResusp treatment, in the V1 simulations.

Figure 3 shows the horizontal distributions of annual surface precipitation rates and column evaporation fractions, for stratiform plus shallow convective (S+SC), and for deep convective clouds. S+SC precipitation patterns are very similar in the V0 and V1 simulations, except V1 has more S+SC precipitation in equatorial regions and less in the N. Hemispheric storm tracks. S+SC evaporation in V0 is much stronger with high evaporation over much of the tropics; high S+SC evaporation in V1 is mostly limited to marine stratus regions and some desert regions where precipitation is low. Deep convective evaporation is generally low, although somewhat greater over land, and is only strong over some desert regions where precipitation is very low. (The V0 deep convective precipitation and evaporation are not shown because V0/V1 differences are not large and the deep convective evaporation has a relatively small contribution to the aerosol resuspension.) Figure 4 shows zonal average distributions for precipitation production and evaporation rates. S+SC production patterns are again similar in V0 and V1, but somewhat stronger in V0. S+SC evaporation in V1 is mostly at 900-1000 hPa, but extends noticeably higher in V0.

4.1.1.3 Aerosol scavenging and resuspension

Table 4 shows the global, annual averages of aerosol wet removal and resuspension from evaporating precipitation for deep convective and stratiform plus shallow convective clouds. The wet removal values are presented as percentages of the total removal (i.e., wet plus dry

removal). Wet removal accounts for 63-89% of the total removal for the predominantly fine aerosol species (SO₄, BC, POA, and SOA), 33-49% for sea salt, and only 23-35% for dust.

The wet removal percentages are somewhat lower in the V1 simulation. Deep convective precipitation accounts for 40-61% of the total wet removal in the V1 simulation, but somewhat less (31-49%) in the V0 simulation.

Resuspension values are presented as percentages of the scavenged amounts (i.e., amounts of aerosol initially captured by precipitation) that are resuspended from evaporating precipitation. For deep convective clouds, the resuspension value is 1% or less. This is considerably lower than the deep-convective precipitation evaporation fractions (5-8%) and is due to the non-linearity in the new-nonlinear resuspension treatment. For the S+SC clouds, the resuspension values are 8-13% in V1 and 23-54% in V0. These V1 resuspension values are lower than the 18% S+SC evaporation fraction in V1 and again is due to the resuspension nonlinearity. In contrast, the V0 resuspension values are more comparable to the 49% S+SC precipitation evaporation in the V0 simulation.

Looking back at the Table 2 results, the much lower sensitivity to the resuspension treatments in V1 than in V0 is attributable to lower evaporation percentages and even lower resuspension percentages for stratiform precipitation, a somewhat greater contribution of deep convective precipitation to the wet removal, and somewhat weaker wet removal overall (relatively to dry-deposition removal).

4.1.1.4 Resuspended particle size

Particles resuspended from evaporating precipitation are expected to be in the coarse-mode size range, but it is of interest to see their actual sizes. Figure 5 shows the horizontal distribution of emitted, ambient, and resuspended volume-mean diameters for coarse-mode particles in the V1 new-nonlinear-resuspension-treatment simulation. Volume-mean diameter is calculated as

$$D_{\text{vol-mean}} = [6 * (\text{mass-mixing-ratio}) / (\pi * \text{density} * (\text{number-mixing-ratio}))]^{1/3}$$

and the ambient and resuspended sizes are vertically-averaged over the tropospheric column.

Average emitted diameters are 2.9 μm over ocean and 3.8 μm over dust source regions.

Ambient diameters are somewhat smaller, averaging 2.4 μm globally, 2.2 μm in sea salt dominated regions, and 2.6 μm in dust dominated regions. The resuspended diameters are larger than the emitted and ambient diameters, averaging 4.1 μm globally, 4.0 μm in sea salt dominated regions, and 5.7 μm in dust dominated regions. The resuspended diameter exceeds 6 μm over African and Asian desert regions and the S. E. Pacific and S. E. Atlantic marine stratus regions. The larger sizes (compared to ambient) can lead to faster dry deposition and below-cloud scavenging and shorter lifetimes for the coarse-mode aerosol.

The resuspended diameter from convective precipitation is larger (5.7 μm average) than for stratiform precipitation (4.0 μm average). The ambient diameter has a weak vertical variation in the troposphere, but the resuspended diameter decreases noticeably above the boundary layer (not shown).

For the V0 new-nonlinear resuspension treatment simulation, the resuspended sizes are considerably larger. They average 7.2 μm globally, 6.2 μm in sea salt dominated regions, and 12.5 μm in dust dominated regions (results not shown). The larger resuspended sizes in the V0 simulation, particularly over dust regions, is caused by higher precipitation evaporation fractions (resulting in more of the larger drops evaporating completely) and the stratiform precipitation being somewhat dirtier (higher kg-dust kg-water⁻¹, that we attribute to differences in the stratiform microphysics).

4.1.2 Evaluation of the new SOA treatment

To evaluate the new SOA treatment in EAMv1 and its impact on the simulated organic aerosol (OA), we use surface OA measurements obtained from different field campaigns in rural/remote areas around the world in 2000-2008 (Jimenez et al., 2009). Although only total

OA (POA+SOA) is measured using instruments such as the Aerosol Mass Spectrometer (AMS), SOA is shown to be associated with oxygenated OA (OOA) factor derived from positive matrix factorization (PMF) analysis (e.g., Zhang et al., 2007). OOA factor has been shown to dominate OA composition, especially in rural areas. Since these measurement data are limited to particles smaller than $1 \mu\text{m}$, we only use model simulated POA and/or SOA in Aitken, accumulation, and primary carbon modes for the comparison. As shown in Fig. 6, the model estimated monthly mean OA (sampled for the same months and locations of the measurements) in CTRL shows a good agreement with the global observed OA concentrations with a normalized mean bias (NMB) of 7%. When the new SOA treatment is excluded in noNewSOA, near-surface OA is largely overestimated (with a NMB of 53%). However, the simulated SOA in noNewSOA (NMB=16%) agrees better with the measured OOA than in CTRL (NMB=-32%), indicating that the elevated injection of SOAG in the new treatment may have overcorrected the positive bias in near-surface OA concentration at these sites.

To verify this at other locations, we also use the Interagency Monitoring of Protected Visual Environments (IMPROVE) program that provides near-surface OC concentrations at many U.S. sites. Here we select 165 rural/remote IMPROVE sites, excluding the ones close to large urban areas. Figure 7 shows the comparison of median value of monthly means at these sites between the model simulations and IMPROVE observations. Observed monthly 15th and 85th percentiles are also shown as boxes to indicate site-to-site variability. Note that model simulated organic matter is converted to an OC concentration using OM:OC ratios of 1.4 for POA and 1.8 for SOA, following the conversion of OC to OA for POA emissions and the treatment of S2015. [Some observed OM:OC ratios are 1.6 for biogenic SOA and 2.1 for rural mixed OA (Turpin and Lim, 2001; Shilling et al., 2009).] Again, the simulated OA in Aitken, accumulation, and primary-carbon modes is used to compare with the measured fine particles. While both simulations capture the seasonal variations of OC at IMPROVE sites, CTRL again

has lower near-surface concentrations throughout the year than noNewSOA, with NMBs of -19% and 21%, respectively.

The SOA column burdens in CTRL are noticeably higher than in noNewSOA (shown in Fig. S1 in the supplement), which is consistent with the differences shown in S2015; between the FragNVSOA and Standard CAM5 distributions in their Figure 2). Global annual SOA burdens are 2.82 and 1.23 Tg for CTRL and noNewSOA, which are fairly close to the corresponding burdens (3.15 and 1.05 Tg) in S2015. However, there are noticeable differences in the contrast of spatial distributions, which can be attributed to the 75% biomass-burning source reduction in the E3SMv1 SOA treatment and to many other differences between the E3SMv1 and the CAM5 version used in S2015. CTRL also has noticeably larger SOA mixing ratios in the mid and upper troposphere compared to noNewSOA (shown in Fig. S2). This is due to having SOAG emissions in the free troposphere in CTRL to mimic the transport of higher volatility SOA precursors (emitted in the lower troposphere) to these altitudes followed by chemical aging and condensation, as explicitly treated in the simulation of S2015.

4.1.3 Evaluation of the new H_2SO_4 time-splitting treatment

According to an AeroCom aerosol microphysics intercomparison study (Mann et al., 2014), simulated CN_{30} is very diverse among the participating models, including CAM5 in which aerosol microphysical treatments are very similar to those in EAMv0. Global mean CN_{30} in CAM5 is much lower than the multi-model mean, although the concentration of accumulation-mode particles is very close to the multi-model mean. Here we calculate the same quantity (CN_{30}) from the CTRL and noNewH₂SO₄ simulations to demonstrate the impact of the new time-splitting approach for H₂SO₄ vapor production/loss. Figures 8 and 9, respectively, show the vertical-meridional distribution and near-surface horizontal distribution of CN_{30} from the two simulations. CN_{30} is much increased globally in the CTRL simulation with the new treatment, compared to noNewH₂SO₄ that uses the old H₂SO₄ treatment as in CAM5. In

noNewH₂SO₄, near-surface CN₃₀ over major continental source regions (except for East Asia and South Asia) is below 2000 cm⁻³, while the new treatment brings CN₃₀ above 2000 cm⁻³ over most areas in central Europe and eastern U.S. as well. There is also a discernible increase in CN₃₀ over biomass burning regions in South America and South Africa and the adjacent oceanic outflow areas. The new treatment also has a strong impact over remote oceans that is presumably associated with new particle formation from the oxidation of dimethyl sulfide (DMS). The comparison of vertical-meridional distributions shows that the impact is not limited to the lower troposphere but also seen in the upper troposphere due to either local nucleation or convective transport. The meridional gradient in CN₃₀ becomes smaller, especially, in the northern hemisphere. The CN₃₀ enhancement occurs not only in the northern hemispheric anthropogenic source regions, but also in the clean oceanic and polar regions, which has an implication for model performance in representing the background aerosol conditions for determining the pre-industrial droplet concentrations and calculation of present-day aerosol indirect forcing. The CN₃₀ results in CTRL are much closer to the multi-model mean results in Mann et al. (2014) than are those in noNewH₂SO₄.

In addition to the comparison with AeroCom models, here we also compare model simulated CN₁₀ in CTRL and noNewH₂SO₄ against in situ measurements at monitoring sites over the globe (Table 1 of Yu and Luo, 2009), shown in Figure 10. CN₁₀ ($D_p > 10$ nm) is selected for comparison due to the measurement size threshold (cut-off diameter of particle counter) being close to the Aitken mode size range in the model. Note that the comparison here is not meant to be quantitatively accurate, since the data duration is not consistent among the sites and with the model time period, but it still provides a useful indication on whether or not the new treatment improves the simulated CN₁₀. The CTRL shows a higher CN₁₀ that is in a better agreement with observations than the noNewH₂SO₄ in terms of the normalized mean bias and correlation coefficient. Over most of the sites the CTRL has a ratio to the

corresponding observed value within a factor of two. Without the new time-splitting approach (noNewH₂SO₄), CN₁₀ at the Europe and N. America sites is largely underestimated. The sites in polar region and free troposphere also show improvements. This is consistent with the global comparison in Figs. 8 and 9. Note the large sensitivity of CN₁₀ to the time-splitting approach in the marine boundary-layer, where the increase in ultrafine particles is directly attributed to the treatment of nucleation of sulfuric acid vapor (originating from DMS).

4.2 Impact of new treatments on aerosol optical depth spatial distribution

The global annual mean total AOD (550 nm) from the E3SMv1 simulation (CTRL) is compared to E3SMv0 (CAM5.3) and observational composite (shown in Fig. 11). Note that both CTRL and CAM5.3 represent one year (2007) while the observational composite based on AeroCom models and ground network measurements is for present-day climatology (Kinne et al., 2013). Thus we also plot AOD from the 15-year (2000-2014) E3SMv1 simulation (CTRL15) for comparison. The global mean AOD in CTRL is a little smaller than in CTRL15 (0.132 vs. 0.143) mostly due to weaker dust loading over north Africa and its oceanic outflow region. Otherwise, the spatial distribution is similar in the two runs. Compared to the observational composite, E3SMv1 overestimates AOD near some desert source regions, but CAM5.3 has an even stronger positive bias in dust loading. This difference is partly due to dust being emitted into a much shallower lowest model layer in E3SMv1 for increased model vertical resolution that leads to more dust dry deposition. E3SMv1 has a clear reduction of low AOD bias over East Asia and the Siberian oceanic outflow area as well as the Arctic (Fig. S3), which is largely attributed to new treatments of NewSOA, NewH₂SO₄, and NewConvTran (Fig. S4). However, there is an overcorrection in oceanic outflow from China and equatorial Africa (Fig. S3), likely due to the new treatment of elevated SOA sources (Fig. S4). Strong sensitivities of SOA loading and lifetime to parameters that characterize aging and chemical reactions of SOA gases are found during the

model development, which is challenging to represent in climate models without explicit treatments of SOA formation.

4.3 Impact of new treatments on aerosol-radiation interaction

The various new treatments in EAMv1 affect the horizontal and vertical distributions of aerosols that can largely influence the impact of aerosols on the atmospheric radiative energy budget through their scattering and absorption of solar and/or terrestrial radiation. Figure 12 shows the impact of individual new treatments on the TOA clear-sky net radiative flux (W m^{-2}) under present-day (PD) aerosol conditions. Among the new treatments, the improved transport and removal (NewConvTran) and the new resuspension of aerosols from evaporation of precipitation (NewResusp) give a net positive (warming) effect, while the new treatments of SOA (NewSOA), sulfuric acid vapor for new particle formation (NewH₂SO₄) and ice nucleation (NewIceNuc) exert a net cooling. Both NewConvTran and NewResusp reduce global mean aerosol loading, but they have different effects on the vertical distribution with NewConvTran reducing more of the upper tropospheric aerosols and NewResusp reducing more of the lower tropospheric aerosols. As discussed in detail by Wang et al. (2013), NewConvTran also increases the transport of aerosols to the remote regions (e.g., the Arctic), which has a further impact on the surface radiation budget through the deposited light-absorbing particles in snow/ice. The strong warming effect over the Arctic by NewConvTran (Fig. 12b) is likely contributed by the additional shortwave heating at the surface. In contrast, the net cooling over north Africa (Fig. 12b) is due to an increase of outgoing longwave radiation associated with reduced dust loading. NewSOA increases SOA lifetime and loading in the upper troposphere, especially over remote oceans and the Arctic, leading to a strong additional shortwave cooling to the present-day climate (-0.64 W m^{-2}). NewIceNuc is the other new treatment that has a strong longwave cooling impact (-0.63 W m^{-2}), mainly over high latitudes and tropics where ice clouds frequently occur.

Figure 13 shows the net clear-sky radiative forcing (i.e., difference between present-day and preindustrial conditions) caused by aerosol-radiation interactions in the atmosphere and light-absorbing particles in snow/ice. A strong radiative cooling is seen over the Arctic and major aerosol source regions (e.g., East Asia, South Asia) and the oceanic outflow areas. A strong positive forcing occurs over northern Africa, western Asia, and the Middle East where light-absorbing dust prevails. This result indicates that dust absorption is increased under the present-day condition due to more dust and/or enhanced absorption, caused by more SOA on dust particles for example. The NewConvTran and NewIceNuc treatments reduce the positive forcing (over northern Africa and western Asia) while the NewH₂SO₄ and NewSOA increase it. Both NewH₂SO₄ and NewIceNuc account for a large portion of the negative forcing over the Arctic. As discussed above, NewSOA increases the direct cooling under present-day aerosol conditions. It also contributes 30% of the global mean clear-sky aerosol forcing (-0.15 out of -0.5 W m⁻²), mostly occurring over oceans.

4.4 Impact of new treatments on aerosol-cloud interactions

Impact of the new treatments on aerosols can alter the global distribution of CCN and their effect on clouds. Figure 14 shows the global distribution of difference in boundary-layer CCN number concentration (at 0.1% supersaturation) between PD and PI aerosol conditions. The increase of PD CCN mostly occurs near major source regions and the oceanic outflow areas. Among the individual new treatments, the NewH₂SO₄ contributes the most to a ubiquitous CCN increase while NewResusp has an opposite effect on CCN. The impact of NewSOA on the CCN increase is strong but also more complicated than the others. The elevated injection of SOAG reduces the contribution of SOA formation to boundary-layer CCN, while SOA formed in the free troposphere is transported further into the oceanic regions and has a far-reaching impact on CCN there. The impact of new treatments on clouds through microphysical processes and/or associated feedbacks manifests itself in the

response of cloud liquid water path (LWP), as shown in Fig. 15. With the combination of all new treatments in EAMv1, the global mean LWP for PD is increased from the PI emission conditions by 2.4 g m^{-2} , primarily in the northern hemisphere where the present-day anthropogenic emission sources are located. The individual new treatments have quite diverse influences on LWP. NewConvTran reduces the LWP difference between PD and PI by -0.8 g m^{-2} while NewH₂SO₄ increases the LWP difference by 0.7 g m^{-2} likely through the conventional second aerosol indirect effect (i.e., more aerosols leading to longer cloud lifetime and larger cloud amount). The impact of NewIceNuc on the PD-PI difference in LWP, involving ice cloud processes, is mainly due to the new treatment of ice formation in mixed-phase clouds (Wang et al., 2014), which increases the amount of liquid cloud and, therefore, the sensitivity to aerosol perturbation over the Arctic. Both NewIceNuc and NewH₂SO₄ seem to account for much of the PD-PI LWP increase over the Arctic. The increase over Eurasia continent is consistent with CCN increase. NewSOA and NewResusp have relatively small impact on the LWP difference.

The global mean total aerosol indirect forcing (-1.1 W m^{-2}) includes the interactions between aerosols and warm clouds as well as ice clouds. As shown in Fig. 16, the spatial distribution of regional cloud radiative cooling is consistent with the increase in CCN and/or LWP. Positive cloud radiative forcing over the Arctic is attributable to NewH₂SO₄ and NewIceNuc changes through longwave warming effect (not shown). NewH₂SO₄ is also responsible for much of the cloud radiative cooling in the northern hemispheric mid-latitudes, where NewConvTran offsets the cooling to some extent, presumably, through both first and second indirect effects. The global total aerosol effective radiative forcing (Fig. S5) is dominated by indirect forcing, although clear-sky aerosol forcing over some regions and contributions by individual treatments are stronger (Fig. 13). The noisy forcing distribution in the tropics for all panels in Fig. 16 reflects a strong variability in the response of deep

convective clouds to the individual new treatments, which becomes weaker in the CTRL simulations when all treatments are combined.

Following Ghan et al. (2016), the change in liquid cloud shortwave radiative forcing (R) as a response to a change in CCN concentrations (N_c) due to anthropogenic aerosol emissions can be decomposed into a chain of processes, involving changes in cloud droplet number concentration (N_d), liquid cloud fraction (C), in-cloud shortwave radiative forcing (R_c), cloud optical depth (τ), droplet effective radius (r_e) and liquid water path (L), as described in the following equations:

$$\Delta\bar{R} = \bar{R} \frac{\Delta\ln\bar{R}}{\Delta\ln\bar{N}_d} \frac{\Delta\ln\bar{N}_d}{\Delta\ln\bar{N}_c} \Delta\ln\bar{N}_c \quad (1)$$

$$\frac{\Delta\ln\bar{R}}{\Delta\ln\bar{N}_d} = \frac{\Delta\ln\bar{C}}{\Delta\ln\bar{N}_d} + \frac{\Delta\ln\bar{R}_c}{\Delta\ln\bar{N}_d} \quad (2)$$

$$\frac{\Delta\ln\bar{\tau}}{\Delta\ln\bar{N}_d} = -\frac{\Delta\ln\bar{r}_e}{\Delta\ln\bar{N}_d} + \frac{\Delta\ln\bar{L}}{\Delta\ln\bar{N}_d} \quad (3)$$

Where the overbar indicate spatiotemporal mean for each quantity, and Δ denotes the difference in the corresponding mean quantity between any pair of PD and PI simulations.

Figure 17 shows the comparison of factors/processes described in Eqs. (1-3) among the various configurations of the EAMv1 model as well as one version of the CAM5 model, CAM5.3_PNNL in Ghan et al. (2016). The CTRL simulation has a much smaller base shortwave cloud radiative forcing R but a larger change (ΔR) than CAM5.3. The comparison suggests that the different ΔR is primarily driven by differences in the CTRL warm cloud radiative forcing R , although there are different sensitivities between N_c , N_d , or R . The lowered base R of warm clouds in EAMv1 likely comes from changes in model vertical resolution, cloud treatments and/or model calibration against satellite-based observations for all clouds (Xie et al., 2018; Rasch et al., 2019). The increased ΔR in EAMv1, compared to CAM5.3, is primarily due to stronger sensitivity to N_d . The various new aerosol treatments EAMv1 do have some impact on ΔR , among which the NewH₂SO₄ treatment has the largest

impact (i.e., contrast between CTRL and noNewH₂SO₄). This is consistent with the large increase in the number concentration of small-size and CCN particles when using the new time-splitting approach for H₂SO₄ vapor production/loss, as shown in Figs. 8 and 9. Although the impact of NewH₂SO₄ on ΔN_c (at the supersaturation of 0.3%) is relatively small, the sensitivity of N_d is substantially enhanced. Further decomposition in Fig. 17b shows that the sensitivity of R to N_d is predominantly from in-cloud forcing (R_c) rather than cloud fraction, particularly for the EAMv1 simulations, although the different aerosol treatments also cause diversity in the sensitivity of both R_c and C to N_d . R_c is determined by cloud optical depth (τ), which is directly connected to cloud microphysical processes that account for the impact of aerosols on droplet size (r_e) and liquid water path (L). The EAMv1 simulations have a much smaller sensitivity in L to N_d but a larger sensitivity in r_e to N_d compared to CAM5 (Fig. 17c), indicating a stronger first indirect effect and weaker second indirect effect in the EAMv1 model. Both NewResusp and NewH₂SO₄ have a discernable impact on aerosol indirect effects.

4.5 BC and dust in snow

The aforementioned changes made to atmospheric aerosols that affect the spatial distribution, droplet/ice nucleation and/or deposition of BC and dust particles also have impacts on their concentration and radiative forcing in snow/ice. Here we analyze some of the simulations listed in Table 1 to quantify such impacts. Figure 18 shows the impact of individual changes on BC concentration in terrestrial surface snow. The NewConvTran has the largest overall impact on BC in snow. There is a decrease of 2.5 ng g⁻¹ in the global annual mean BC concentration (compared to the difference of 21.5 ng g⁻¹ due to the present-day emission changes from pre-industrial conditions). The NewConvTran treatment reduces wet deposition of BC in low to mid-latitude source regions and moves more to the high latitudes, so the impact is larger in the colder months of the northern hemisphere when mid-latitudes have

more seasonal snow cover. The NewSOA increases the lifetime of SOA as well as BC and POA that share similar sources and the soluble size modes, allowing for more BC to move to mid- to high-latitude snow-covered areas. NewResusp removes more BC near source regions, having a negative impact on remote BC in the atmosphere as well as in snow. The impact of NewIceNuc and NewH₂SO₄ on BC in snow is less straightforward with larger intra-seasonal variability in both magnitude and sign than the other new treatments but the overall positive impact on annual mean value (+0.22 and +0.14 ng g⁻¹ for NewIceNuc and NewH₂SO₄, respectively) is consistent with their impact on atmospheric aerosols or CCN (see Fig. 14).

The direct improvement to the model representation of BC/dust mixing with snow grains and their optical properties can be assessed with the NewInSnow results (i.e., difference between the CTRL and noNewInSnow simulations), as shown in Fig. 19. The combination of NewInSnow treatments introduces a global annual mean positive SW radiative forcing of 0.26 W m⁻² at the surface under the present-day conditions, predominantly at high latitudes of both hemispheres. The global mean forcing peaks in boreal winter months (up to 0.6 W m⁻²; see Fig. S6) when the northern hemisphere has large seasonal terrestrial snow cover and the Antarctic ice sheet receives strongest incoming solar radiation. The forcing under clear sky (Fig. 19b) is larger and less ambiguous than in all sky (Fig. 19a) where negative forcing is seen over some oceanic areas. NewInSnow has no direct impact on the atmospheric radiative transfer, so the SW forcing at TOA (under both clear and all sky conditions) is indistinguishable from that at the surface (not shown). The additional heating caused by NewInSnow leads to an increase of 0.04 K in global mean surface temperature, with local increases over 0.5 K at high latitudes, and a decrease of 0.55 mm in global mean snow water equivalent. The increase in surface temperature can cause increases in the outgoing LW radiation, sensible and latent heat fluxes at the surface, which can partly offset the positive SW radiative flux (Fig. 19c, d). Interestingly, although global mean net energy flux at the

surface is not much reduced after the adjustment of LW radiation and sensible/latent heat release, the net heating to the surface is shifted from land to ocean through reduced latent and sensible heat fluxes.

5. Summary and Conclusions

There are substantial new developments in various components of E3SMv1 to represent aerosols and light-absorbing impurities as well as their interactions with clouds and radiation on top of CESM1.3 (referred to as E3SMv0), aimed at reducing some known biases or correcting model deficiencies. In this study we summarize what the new treatments are and how they affect aerosols and radiative forcing in E3SMv1, both individually and collectively.

The notable new treatments include:

- 1) A new treatment of H_2SO_4 vapor for new particle formation (denoted as NewH₂SO₄) uses a parallel time-splitting approach (rather than the serial time-splitting approach in E3SMv0) to provide more accurate H_2SO_4 vapor concentrations to the aerosol nucleation.
- 2) A suite of improved treatments of convective transport and aerosol wet removal (denoted as NewConvTran), based on Wang et al. (2013), is introduced to E3SMv1 to get a better simulation of aerosol spatial distributions.
- 3) A new treatment of SOA (denoted as NewSOA) uses SOA gas emissions derived from results based on an explicit treatment of SOA precursor-gas chemistry and particle-phase transformation that was computationally expensive but more accurate (Shrivastava et al., 2015).
- 4) A new treatment of marine organic aerosol (denoted as NewMOA) is introduced to E3SMv1 to account for organic sea-spray emissions, assuming an internal mixing with the co-emitted inorganic sea salt (Burrows et al., 2014, 2018).

- 5) A new ice-nucleation treatment (NewIceNuc) that links the heterogeneous ice formation in mixed-phase clouds to both interstitial and cloud-borne dust and black carbon aerosols (Wang et al., 2014) is adopted. Moreover, threshold size (a constant-valued tunable parameter) at which growing ice crystals are converted to snow particles is replaced with an empirical formulation that treats the size as a function of temperature in EAMv1.
- 6) A new treatment of resuspension of aerosol material from evaporating precipitation (NewResusp) is developed that remedies two shortcomings of the original MAM treatment of this process, which is for the first time tested in both E3SMv1 and E3SMv0. Aerosol material is now resuspended to the coarse mode, rather than to the mode from which it was scavenged. The fraction of precipitation-borne aerosol material that is resuspended is now a nonlinear function of the fraction of precipitation mass-flux that evaporates (developed from a simple spectral-bin model of raindrop evaporation below cloud base). The number of resuspended aerosol particles, which together with resuspended mass determines the size of the resuspended particles, is equal to the number of fully evaporated raindrops. This is also parameterized as a nonlinear function of the fraction of precipitation mass-flux that evaporates.
- 7) A set of new treatments of light-absorbing particles (NewInSnow) in surface snow and sea ice is introduced to E3SMv1 to improve the consistency with deposition mechanisms of atmospheric aerosols, including the consideration of within-hydrometeor light-absorbing particles (Flanner et al., 2012).

Among these seven sets of new treatments, four of them (i.e., NewH₂SO₄, NewSOA, NewResusp and NewInSnow) have never been specifically evaluated and assessed in the E3SMv1 framework. Thus our model evaluation is particularly focused on these.

The new time-splitting approach for H₂SO₄ vapor production/loss (NewH₂SO₄) largely increases the amount of small particles ($D_p > 10$ nm) over the entire globe, which agrees much better with observations and the AeroCom multi-model mean. The NewH₂SO₄ treatment also substantially increases the PD-PI contrast of mid-/high-latitude CCN concentrations, liquid water path and the cloud radiative cooling in the northern hemisphere.

The new SOA treatment (NewSOA) increases the lifetime and column burden of SOA, especially in the upper troposphere and over remote oceans and the Arctic. The NewSOA treatment contributes substantially to regional total AOD and global mean clear-sky radiative cooling (-0.15 out of -0.5 W m⁻²). It reduces the low bias in E3SMv0 AOD, compared to the observational composite, over heavily polluted regions (e.g., East Asia, South Asia, and South America biomass burning areas), but it overcorrects the bias over some remote oceans. The NewSOA does increase the present-day CCN but has a minimal impact on clouds and aerosol indirect forcing.

The new resuspension treatment (NewResusp) produces a modest reduction in aerosol mass and number concentrations, AOD, CCN, and cloud droplet number in the EAMv1 model. This is due to the resuspended aerosol being in the coarse mode where particle lifetime is shorter, and the nonlinear aspect of the resuspension parameterization. In the EAMv0 (or CAM5.3) model, where evaporation of stratiform precipitation is much stronger (presumably due to using the original MG cloud microphysics rather than the newer MG2), the new resuspension treatment produces reductions of over 30% for AOD, CCN, and cloud droplet number. This indicates that the importance of the resuspension from evaporating precipitation process can differ strongly between global models or model versions, depending on the model physics. The resuspended particles are larger than the ambient coarse-mode particles: the global-average volume-mean dry diameter of the resuspended particles is 4.1 μm in EAMv1 and 7.2 μm in EAMv0, compared to 2.4 μm for ambient coarse-mode

particles. A linearized version of the new resuspension treatment, in which both the fraction of aerosol material resuspended and the fraction of raindrops that fully evaporate are assumed equal to the fraction of precipitation mass-flux that evaporates, gives results quite close to those with the new nonlinear resuspension treatment and thus is a reasonable alternative approach.

The changes made to atmospheric aerosols that affect the spatial distribution and deposition of BC and dust particles also have impacts on their concentration and radiative forcing in snow/ice. The improved transport and removal (NewConvTran) has the largest overall impact on BC concentrations in snow, while the combination of NewInSnow treatments introduces a global annual mean positive SW radiative forcing of 0.26 W m^{-2} at the surface under the present-day conditions, predominantly at high latitudes of both hemispheres. The additional heating caused by NewInSnow leads to an increase of 0.04 K in global mean surface temperature, with local increases over 0.5 K at high latitudes, and a decrease of 0.55 mm in global mean snow water equivalent.

With all the new aerosol treatments, the low-resolution EAMv1 (30 spectral elements or 1°) gives a fairly low global mean aerosol indirect forcing (-1.1 W m^{-2}), although the total effective radiative forcing of -1.6 W m^{-2} (including -0.5 W m^{-2} as the clear-sky radiative forcing) is still too high for the model to reproduce the historical warming trend (Golaz et al., 2019). The EAMv1 has a much smaller sensitivity in liquid cloud water but a larger sensitivity in cloud drop size to changes in cloud drop number compared to EAMv0, indicating a stronger first indirect effect and a weaker second indirect effect in the EAMv1 model. Some of the individual new treatments (e.g., NewResusp and NewH₂SO₄) have a discernible impact on aerosol indirect effects. The representation of aerosol-cloud interactions in E3SMv1 has also been evaluated and further improved from the cloud perspective (e.g., Rasch et al., 2019). While preparing for further aerosol developments in

next-generation E3SM to remove some known biases (e.g., in dust loading/deposition and SOA formation) and/or to add new capabilities (e.g., representation of nitrate aerosol and stratospheric sulfate), we keep evaluating their impact on the aerosol effective radiative forcing to identify and reduce potential uncertainties.

Appendix A: Raindrop Spectrum Evolution During Evaporation

Here we present some calculations of raindrops evaporating (and resuspending aerosol particles) as they fall through sub-saturated air below cloud base. These results are then used to derive simple parameterizations of the resuspension of rain-borne aerosol mass and number for use in the global climate model. The calculations, which are relatively straightforward, are made using a one-dimensional steady-state model with a size-resolved representation (i.e., spectral bin) of the raindrop size distribution. The model is similar to that used in some early studies of below-cloud aerosol scavenging and evaporation (Abraham et al., 1972; Stensland and de Pena, 1975), but is simpler as it only treats the evaporation process.

Raindrops fall from cloud base ($z = z_{cb}$) to the surface ($z = z_{sfc} = 0$). Relative humidity (RH) varies linearly from a specified surface value to 100% at cloud base. Temperature (T) is 298 K at the surface, and lapse rate is -6.5 K km^{-1} . Pressure (p) is 10^5 Pa at the surface and is calculated from the hydrostatic equation above the surface.

The precipitation rate at cloud base, $J(z_{cb})$ (mm h^{-1}), is specified, giving a precipitation water flux of $FW(z_{cb}) = J(z_{cb})/3600$ ($\text{kg m}^{-2} \text{ s}^{-1}$). (Note that the sign convention for all precipitation related fluxes and fall speeds is positive downwards throughout the paper.) An initial (cloud base) raindrop size distribution is calculated assuming either a Marshall-Palmer (MP) or lognormal (LN) size distribution. The Marshall Palmer size distribution (Marshall and Palmer, 1948) is

$$\frac{dN}{dD} = N_0 e^{-\lambda D} \quad (\text{A1})$$

where D is drop diameter (m), N_0 (m^{-4}) = 8.0×10^6 , and $\lambda(\text{m}^{-1}) = 4100 J^{0.21}$. The lognormal size distribution is

$$\frac{dN}{dln(D)} = \frac{N_{tot}}{\sqrt{2\pi ln(\sigma_g)}} exp \left\{ -\frac{1}{2} [ln(D/D_{gn})/ln(\sigma_g)]^2 \right\} \quad (\text{A2})$$

The 3 lognormal parameters are taken from empirical fits of Harikumar et al. (2009): N_{tot} (m^{-3}) = $\exp[5.2147 - 0.0072J + 0.3575\ln(J)]$, D_{gn} (m) = $\exp[-6.4726 + 0.0006J + 0.2011\ln(J)]$, and σ_g = 1.5011. We discretize the distribution using 500 logarithmically spaced droplet size

bins with droplet radii between 25 μm and 5.0 mm. Thus at cloud base, $R_j(z_{cb})$ (m) is the drop radius and $N_j(z_{cb})$ (m^{-3}) is the raindrop number concentration in size bin j . The precipitation water flux is re-calculated from these $N_j(z_{cb})$ using

$$FW = \sum_j (4\pi\rho_w/3)R_j^3 V(R_j, \rho_a)N_j \quad (\text{A3})$$

where $V(R_j, \rho_a)$ is the raindrop fallspeed (m s^{-1}), ρ_a is air density (kg m^{-3}), and ρ_w is water density (1000 kg m^{-3}). FW will differ somewhat from the specified $FW(z_{cb})$, so these first-guess $N_j(z_{cb})$ are scaled so as to produce the specified water flux exactly. Raindrop number flux $FN(z_{cb})$ ($\text{m}^{-2} \text{ s}^{-1}$) is then

$$FN = \sum_j V(R_j, \rho_a)N_j \quad (\text{A4})$$

At cloud base, all drops are assumed to have an identical aqueous concentration of aerosol material, C_{aq-cb} ($\text{kg-aerosol kg-water}^{-1}$). The mass of aerosol material in a single droplet in size bin j , AM_j (kg-aerosol), is then

$$AM_j = C_{aq-cb}(4\pi\rho_w/3)R_j^3 \quad (\text{A5})$$

and this value does not change as a drop evaporates. The rain-borne aerosol mass flux $FA(z_{cb})$ ($\text{kg m}^{-2} \text{ s}^{-1}$) is

$$FA = \sum_j V(R_j, \rho_a)AM_jN_j \quad (\text{A6})$$

This completes the initialization of a calculation for a specified cloud-base height, precipitation rate, and surface relative humidity. We next calculate the evolution of drops in each size bin as they fall through sub-saturated air. This is done by integrating (downwards in z)

$$\frac{d(R_j^2)}{dz} = \left[-\frac{1}{V(R_j)}\right] \frac{d(R_j^2)}{dt} \quad (\text{A7})$$

where

$$\frac{d(R_j^2)}{dt} = f[R_j, AM_j, V, T, p, RH] \quad (\text{A8})$$

is a standard expression for droplet condensation/evaporation. For this we use equation 7.18 of Rogers and Yau (1989) with their ventilation effect correction. The integration is done using a small dz (0.1 m). Until the drops in a bin fully evaporate, the drop number flux remains constant, so that

$$N_j(z) = N_j(z_{cb})V[R_j(z_{cb}), \rho_a(z_{cb})]/V[R_j(z), \rho_a(z)] \quad (\text{A9})$$

The rain-borne aerosol mass flux also remains constant until the bin fully evaporates. When $R_j(z)$ reaches 10 μm , the droplets in bin j are treated as having fully evaporated. The aerosol mass in the bin is resuspended as interstitial aerosol, and the number of resuspended

aerosol particles is equal to the number of drops in the bin. The N_j and AM_j are then set to zero. As one moves downwards in height, the precipitation water flux FW decreases continuously as the droplets in each size bin gradually decrease in size. In contrast, the droplet number flux FN and rain-borne aerosol mass flux FA change in discrete steps, at heights where the drops in a bin reach $10 \mu\text{m}$ radius and are completely evaporated. The 3 fluxes are saved at 50 m height intervals for analysis.

The results from a calculation can be summarized using the fractions of the initial cloud-base fluxes that have been lost through evaporation and resuspension. These evaporated (or resuspended) fractions are define as

$$f_{EV-X}(z) = 1 - FX(z)/FX(z_{cb}) \quad (\text{A10})$$

where X is either W (precipitation water), A (rain-borne aerosol mass), or N (raindrop number). Figure A1 shows calculation results for cloud-base precipitation rates of 0.1, 1.0, and 10 mm h^{-1} , surface relative humidities of 30%, 40%, ..., 90%, and cloud-base heights of 0.5, 1.0, ..., 3.0 km for the two size distribution cases. We plot f_{EV-A} and f_{EV-N} versus f_{EV-W} to show how the resuspension fractions for aerosol mass and number vary with the water mass evaporation fraction.

The results for aerosol mass resuspension are what one might expect. The aerosol mass resuspension is below the 1:1 line, because raindrops can partially evaporate without resuspending any rain-borne aerosol. The aerosol mass resuspension is lower (slower) at higher precipitation rates, because the size distributions at higher rates contain more larger-sized drops, and larger-sized drops take longer to fully evaporate. Similarly, the aerosol mass resuspension for the lognormal distribution gives somewhat slower resuspension than Marshall Palmer because it has more larger-sized drops in comparison to Marshall Palmer. For a particular size distribution type and precipitation rate, different surface relative humidities and cloud-base heights produce different f_{EV-A} (and f_{EV-W}) versus z results. Somewhat surprisingly, however, the f_{EV-A} versus f_{EV-W} points lie within a very narrow envelope. This suggests that, for example, at height below cloud at which drops with initial radii of 0.2 mm completely evaporate (and drops with smaller initial radii have already evaporated), the radii (and degree of evaporation) of drops with initial radii $> 0.2 \text{ mm}$ are relatively independent of the humidity profile through which they have fallen.

The results for drop (and thus aerosol) number resuspension are somewhat more complex. The number resuspension fractions are always greater than the aerosol mass

resuspension fractions, because the smallest drops (which evaporate first) contribute relatively more to the droplet number flux than to the aerosol mass flux. Differences between the Marshall Palmer and lognormal distributions are stronger than for aerosol mass. The Marshall Palmer has a much higher f_{EV-N} at low f_{EV-W} than does the lognormal. This is again due to the Marshall Palmer having relatively more smaller-size drops and fewer larger-sized drops. For a particular size distribution type and precipitation rate, the f_{EV-A} versus f_{EV-W} points again lie within a very narrow envelope.

Figure A2 shows similar results, but for 15 (logarithmically spaced) cloud-base precipitation rates of 0.01 to 31.8 mm h⁻¹. Also shown are 9th-order polynomial curve fits to the results. (The individual data points from the calculations were first aggregated to f_{EV-W} intervals of width 0.01. The averaged f_{EV-A} (or f_{EV-N}) and f_{EV-W} for each interval were then used for curve fitting. This produced better results at high f_{EV-W} values, where there are fewer individual data points.) The normalized root-mean-square error of the fitted curve against the non-aggregated points is between 0.10 and 0.12. Note that results shown in Figure A1 suggest that more accurate fitted curves could be obtained by including the dependence on cloud-base precipitation rate, but this has not been pursued.

These fitted curves represent a parameterization of f_{EV-A} (and f_{EV-N}) as a function of f_{EV-W} , and can be written as:

$$f_{EV-A} = \phi_A(f_{EV-W}) \quad (\text{A11})$$

$$f_{EV-N} = \phi_N(f_{EV-W}) \quad (\text{A12})$$

The 9th-order polynomial coefficients [$\phi(x) = a_1 \cdot x + \dots + a_9 \cdot x^9$, $x = f_{EV-W}$] are given in Table A1. For small values of x , the fitted polynomials are not monotonic, so $\phi(x) = b_2 \cdot x$ is used when $x < b_1$.

It is convenient to express this parameterization in terms of the un-evaporated (or un-resuspended) fractions

$$f_{UE-S} = 1 - f_{EV-S} \quad (\text{A13})$$

where $S = W, A$, or N . Then

$$f_{UE-A} = \psi_A(f_{UE-W}) = 1 - \phi_A(1 - f_{EV-W}) \quad (\text{A14})$$

$$f_{UE-N} = \psi_N(f_{UE-W}) = 1 - \phi_N(1 - f_{EV-W}) \quad (\text{A15})$$

As described in Appendix B, these are used in new the treatment of aerosol resuspension from evaporating precipitation.

Appendix B: New Treatments of Aerosol Resuspension from Precipitation

1) Treatment for stratiform precipitation

We first describe the treatment for stratiform precipitation. The treatment for convective precipitation is similar but has some additional complications.

Let FW_k be the grid-cell mean precipitation water-mass flux at the top of model layer k ($\text{kg m}^{-2} \text{s}^{-1}$) and is positive downwards here. (The vertical layer indexing follows the CAM5.3 and EAMv1 convention of $k=1$ being the uppermost layer, and k increasing with increasing pressure.) In the aerosol wet-removal code, we calculate

$$FW_{k+1} = FW_k + (WPROD_k - WEVAP_k) (\Delta p_k / g) \quad (\text{B1})$$

where $WPROD_k$ and $WEVAP_k$ are the precipitation production and evaporation rates, respectively, in layer k ($\text{kg kg}^{-1} \text{s}^{-1}$, both positive). These are provided by the stratiform cloud parameterization, averaged over the model time-step.

FA_k is the grid-cell mean precipitation-borne aerosol-mass flux for a particular MAM4 aerosol-mass species at the top of layer k ($\text{kg m}^{-2} \text{s}^{-1}$). Here the species includes the chemical component (e.g., sulfate, sea-salt, dust, etc.), the aerosol mode, and the aerosol attachment state prior to scavenging by precipitation (interstitial or cloud-borne). In the aerosol wet-removal code, we calculate

$$FA_{k+1} = FA_k + (ASCAV_k - ARESU_k) (\Delta p_k / g) \quad (\text{B2})$$

where $ASCAV_k$ is the aerosol-mass precipitation-scavenging rate in layer k , and A_RESU_k is the rate of precipitation-borne aerosol-mass resuspension (both $\text{kg kg}^{-1} \text{s}^{-1}$ and positive). The scavenging rate is expressed as

$$ASCAV_k = \lambda_k q_{A,k} \quad (\text{B3})$$

where λ_k is a first-order scavenging rate coefficient (s^{-1}) and $q_{A,k}$ is the aerosol mass-mixing-ratio in layer k (kg kg^{-1}). For cloud-borne aerosol species, the scavenging rate represents the conversion or collection of cloud water to precipitation, which is provided by the stratiform

cloud parameterization. This is referred to as in-cloud scavenging in Liu et al. (2012) and the Fig. 1. For interstitial aerosol species, the scavenging rate represents aerosol particle scavenging by precipitation via Brownian diffusion, impaction, and interception, and the parameterization of Slinn (1984; also see SI of Liu et al., 2012) is used. This is referred to as below-cloud scavenging in Liu et al. (2012) and diffusion/impaction scavenging in Fig. 1, although it also occurs within clouds.

The resuspension rate is expressed as

$$ARESU_k (\Delta p_k / g) = f_{ARESU,k} FA_k \quad (B4)$$

where f_{aresu_k} is the (dimensionless) fraction of precipitation-borne aerosol-mass flux at the top of the layer that is resuspended through precipitation evaporation. Note that this assumes that any aerosol-mass scavenged in layer k is not resuspended in layer k . The original MAM4 treatment for CAM5.3 assumes that the precipitation-borne aerosol-mass resuspension is proportional to the precipitation water evaporation, so

$$f_{ARESU,k} = (WEVAP_k \Delta p_k / g) / FW_k \quad (B5)$$

The original MAM4 treatment also places the resuspended aerosol mass in the originating mode. E.g., Aitken-mode sulfate that is precipitation-scavenging then resuspended in a lower model layer is placed in the Aitken mode in the resuspending layer.

The new treatment places the resuspended aerosol mass in the coarse mode, and uses a more physically-based parameterization of $f_{ARESU,k}$ based on the results described in Appendix A. To explain the new $f_{ARESU,k}$ treatment, first consider a case with a well-defined cloud-base at the top of layer k_base , so that $WEVAP_k = 0$ for $k < k_base$, and $WPROD_k = 0$ for $k \geq k_base$. Also, ignore (for the moment) any aerosol scavenging that might occur below the cloud base. Then, using the notation similar to Appendix A, we have.

$$f_{UE-W,k} = FW_k / FW_{k_base}$$

(B6)

is the fraction of un-evaporated precipitation water at the top of layer k . Similarly,

$$f_{UE-A,k} = FA_k / FA_{k_base}$$

(B7)

is the fraction of un-resuspended precipitation-borne aerosol-mass at the top of layer k , and it follows the functional parameterization of

$$f_{UE-A,k} = \psi_A(f_{UE-W,k})$$

(B8)

These previous two equations can be combined to give

$$FA_{k+1} = FA_k [\psi_A(f_{UE-W,k+1}) / \psi_A(f_{UE-W,k})]$$

(B9)

Finally, because we are ignoring possible below-cloud scavenging,

$$(FA_k - FA_{k+1}) = f_{ARESU,k} FA_k$$

(B10)

so

$$f_{ARESU,k} = 1 - [\psi_A(f_{UE-W,k+1}) / \psi_A(f_{UE-W,k})]$$

(B11)

This provides an expression for $f_{ARESU,k}$ (and also $ARESU_k$) for the well-defined cloud-base case that does not involve FA_{k_base} . It can also be used when below-cloud scavenging is not ignored. In this case,

$$FA_{k+1} = -f_{ARESU,k} FA_k + (ASCAV_k \Delta p_k / g)$$

(B12)

but aerosol-mass scavenged in layer k will undergo resuspension in layers $k+1, k+2, \dots$ following the relation given in (B11) above. Also note that (B5) used in the original MAM4 treatment is equivalent to (B11) if ψ_A is assumed to be linear [$\psi_A(x) = x$].

Unfortunately, this well-defined cloud-base scenario is often not the case.

Simultaneous precipitation production and evaporation in a layer frequently occur, because the stratiform cloud fraction changes between vertical layers. The raindrop spectrum evolution becomes more complicated, and the parameterization developed in Appendix A does not strictly apply. Rather than attempting to develop a parameterization for more

complex cloud geometries, the well-defined cloud-base approach above was extended (in an ad hoc manner) as follows:

$$FW_{source,k}^* = \sum_{k' < k} (WPROD_{k'} \Delta p_{k'}/g)$$

(B13)

$$f_{UE-W,k}^* = FW_k / FW_{source,k}^* \quad (B14)$$

$$f_{UE-W,tmp,k}^* = (FW_k - WEVAP_k \Delta p_k/g) / FW_{source,k}^* \quad (B15)$$

$$f_{ARESU,k}^* = 1 - [\psi_A(f_{UE-W,tmp,k}^*) / \psi_A(f_{UE-W,k}^*)] \quad (B16)$$

The main difference between (B6 and B11) and these extended equations (B13-B16) is that the precipitation production above layer k ($FW_{source,k}^*$) replaces the cloud-base precipitation. For the well-defined cloud-base scenario, the extended equations are identical to (B6 and B11).

In the original MAM4 approach, the scavenging and resuspension calculations for aerosol number for each mode are identical to those for aerosol mass, except that the scavenging rate coefficients (λ_k) are somewhat different for aerosol number and mass. In the new treatment, aerosol number is scavenged as in the original treatment, but conceptually there is no precipitation-borne aerosol number. I.e., when an interstitial or cloud-borne aerosol particle is scavenged, its mass is conserved (and becomes precipitation-borne), but its number is forgotten, since the particle is intermixed with other scavenged particles within a given raindrop. The resuspension of aerosol number is determined by the number of raindrops that totally evaporate in the layer, following the Appendix A approach.

Let FN_k be the grid-cell mean raindrop number flux at the top of model layer k ($\# \text{ m}^{-2} \text{ s}^{-1}$, positive downwards). In the aerosol wet-removal code, we calculate

$$FN_{k+1} = FN_k + (NPROD_k - NEVAP_k) (\Delta p_k/g) \quad (B17)$$

where $NPROD_k$ and $NEVAP_k$ are the raindrop number production and evaporation rates, respectively, in layer k ($\# \text{ kg}^{-1} \text{ s}^{-1}$). We again start with the well-defined cloud-base scenario.

For layers above the cloud base (where $NEVAP_k = 0$), FN_k is calculated from the Marshall Palmer size distribution described in Appendix A

$$FN_k = cldf_{k-1} \eta_{MP}(FW_k / cldf_{k-1}) \quad (B18)$$

where $\eta_{MP}(FW)$ is the Marshall Palmer raindrop number flux for a given precipitation flux, and $cldf$ is the stratiform cloud fraction. Thus the in-cloud number flux is calculated from the in-cloud precipitation flux, then is converted to a grid-cell mean. This effectively gives

$$NPROD_k \Delta p_k/g = cldf_k \eta_{MP}(FW_{k+1} / cldf_k) - cldf_{k-1} \eta_{MP}(FW_k / cldf_{k-1}) \quad (B19)$$

For layers below the cloud base (where $NPROD_k = 0$), we write

$$NEVAP_k \Delta p_k/g = f_{NEVAP,k} FN_k \quad (B20)$$

where $f_{NEVAP,k}$ is the fraction of raindrops entering layer k that fully evaporate within that layer. Using the results from Appendix A, and repeating the (B6-B11) derivation with FN rather than FA , we then obtain

$$f_{NEVAP,k} = 1 - [\psi_N(f_{UE-W,k+1}) / \psi_N(f_{UE-W,k})] \quad (B21)$$

For more complex cloud geometries where precipitation production and evaporation occur simultaneously in some layers, we again use an ad hoc extension of these well-defined cloud-base equations. The number production is calculated as

$$NPROD_k \Delta p_k/g = cldf_k \eta_{MP}(FW_{source,k+1}^* / cldf_k) - cldf_{k-1} \eta_{MP}(FW_{source,k}^* / cldf_{k-1}) \quad (B22)$$

with $FW_{source,k}^*$ defined previously. The raindrop number evaporation fraction is calculated as

$$f_{NEVAP,k}^* = 1 - [\psi_N(f_{UE-W,tmp,k}^*) / \psi_N(f_{UE-W,k}^*)] \quad (B23)$$

For a well-defined cloud-base scenario, these extended equations (B22 and B23) are equivalent to (B19 and B21).

The ψ_A , ψ_N , and η_{MP} results from Appendix A, which were derived for rain, are used in resuspension calculations for both rain and snow. Given that aerosol concentrations are higher in the lower (and warmer) troposphere, and ice saturation mixing ratios (which determine snow sublimation) are lower than those for water, this seemed reasonable. However, the amounts of evaporation and associated aerosol resuspension for snow vs. rain in the model have not been investigated. The new resuspension treatment has been implemented with MAM4 and MAM3. Implementation with MAM7 will require assumptions about how the resuspended aerosol is partitioned between the coarse dust mode and coarse sea-salt mode.

A linearized version of the new resuspension treatment has also been implemented, in order to evaluate the impact of the non-linear dependence of FA and FN on FW . It differs from the derivation above only in that the parameterized curve-fits for ψ_A and ψ_N are replaced with identity functions: $\psi_A(x) = x$ and $\psi_N(x) = x$. This simplifies the equations somewhat, so that (B16) and (B23) become

$$f^*_{ARESU,k} = f^*_{NEVAP,k} = (\text{WEVAP}_k \Delta p_k / g) / FW_k \quad (\text{B24})$$

However, the $FW^*_{source,k}$ is still needed for (B22).

2) Treatment for convective precipitation

The treatment for convective precipitation has some differences resulting from the convective cloud geometry (updrafts and downdrafts) and strong updraft speeds. The EAMv0 had separate parameterizations of shallow and deep convective clouds. In EAMv1, the shallow convective and stratiform clouds are both treated (and not distinguished) in the CLUBB parameterization, so there is only a deep convective cloud parameterization.

In the convective wet removal calculations, we assume that precipitation formation and in-cloud scavenging of convective-cloud-borne aerosol mass occur in the updraft.

Resuspension from evaporating precipitation and scavenging of interstitial aerosol mass (by Brownian diffusion and impaction) are assumed to occur in the quiescent environment. Applying these within the convective downdrafts might be more realistic and could be done. However, evaporation and resuspension for convective precipitation are much less than for stratiform precipitation in the model, and the convective parameterization itself provides limited information regarding cloud geometry and microphysics, so improving on the current implementation is not considered a high priority.

The scavenging of interstitial aerosol mass and associated resuspension are calculated as for stratiform precipitation, by solving (B1-B4 and B13-B16) from cloud top to the surface. However, precipitation production and evaporation information from the deep convection parameterization are used, along with the lognormal raindrop distribution results from Appendix A. For convective-cloud-borne aerosol mass, vertical transport, entrainment/detrainment, activation, and scavenging in the updraft are calculated together following Wang et al. (2013, see Supplement). These calculations are done in an upwards sequence (from the surface to cloud top), and they provide the ASCAV_k needed for the resuspension calculations. Resuspension of aerosol mass is then calculated by solving (B1-B4 and B13-B16) from cloud top to the surface. Evaporation of raindrop number is calculated as for stratiform precipitation.

Acknowledgments. This research is based on work supported by the U.S. Department of Energy (DOE), Office of Science, Office of Biological and Environmental Research (BER), Earth and Environmental System Modeling (EESM) program as part of the Energy Exascale Earth System Model (E3SM) project. The authors thank all the E3SM project team members for their efforts in developing and supporting the E3SM. The Pacific Northwest National Laboratory (PNNL) is operated for DOE by Battelle Memorial Institute under contract DE-AC05-76RLO1830. Work at LLNL was performed under the auspices of the US DOE by Lawrence Livermore National Laboratory under contract No. DE-AC52-07NA27344. M. Shrivastava was also supported by the DOE, Office of Science, BER through the Early Career Research Program. J.-H. Yoon was supported by National Research Foundation Grant NRF_2017R1A2b4007480. Computational resources were provided by the National Energy Research Scientific Computing Center, a DOE User Facility supported by the Office of Science under Contract No. DE-AC02-05CH11231, and EMSL Molecular Sciences Computing resources located at PNNL. The E3SMv1 model has been publicly released.

Code and Data Availability

The E3SM project, code, simulation configurations, and tools to work with the output are described at the E3SM website (<https://e3sm.org>). All model codes may be accessed on the GitHub repository (at <https://github.com/E3SM-Project/> or <http://dx.doi.org/10.11578/E3SM/dc.20180418.36>). Specific model simulation used in this study will be made available online (at <http://portal.nersc.gov/>)

References

- Abdul-Razzak, H., and S. J. Ghan (2000), A parameterization of aerosol activation: 2. Multiple aerosol types, *J. Geophys. Res.*, 105(D5), 6837–6844, doi:10.1029/1999JD901161.
- Abraham, F. F., S. K. Jordon, R. N. Kortzeborn, and H. G. Kolsky (1972), Model for time-dependent raindrop size distributions; Application to the washout of airborne contaminants, *IBM J. Res. Develop.*, 16, 91–100.
- Bogenschutz, P. A., A. Gettelman, H. Morrison, V. E. Larson, C. Craig, and D. P. Schanen (2013), Higher-order turbulence closure and its impact on climate simulations in the Community Atmosphere Model, *J. Clim.*, 26, 9655–9676, doi:10.1175/JCLI-D-13-00075.1.
- Bond, T. C., et al. (2013), Bounding the role of black carbon in the climate system: A scientific assessment, *J. Geophys. Res. Atmos.*, 118, 5380–5552, doi:10.1002/jgrd.50171.
- Boucher, O., et al. (2013), Clouds and Aerosols, in Climate Change 2013: The Physical Science Basis. Contribution of Working Group 1 to the Fifth Assessment Report of the Intergovernmental Panel on Climate Change, edited by T. F. Stocker et al., pp. 571–657, Cambridge Univ. Press, Cambridge, U. K., and New York.
- Burrows, S. M., O. Ogunro, A. A. Frossard, L. M. Russell, P. J. Rasch, and S. M. Elliott (2014), A physically based framework for modeling the organic fractionation of sea spray aerosol from bubble film Langmuir equilibria, *Atmos. Chem. Phys.*, 14(24), 13,601–13,629, doi:10.5194/acp-14-13601-2014.
- Burrows, S. M., Easter, R., Liu, X., Ma, P. L., Wang, H., Elliott, S. M., Singh, B., Zhang, K., & Rasch, P. J. (2018). OCEANFILMS sea-spray organic aerosol emissions—Part 1: Implementation and impacts on clouds. *Atmospheric Chemistry and Physics Discussions*, 1–27. <https://doi.org/10.5194/acp-2018-70>
- Carslaw, K. S., et al. (2013), Large contribution of natural aerosols to uncertainty in indirect forcing, *Nature*, 503, 67–71.
- Dang, C., Warren, S. G., Fu, Q., Doherty, S. J., & Sturm, M. (2017). Measurements of light-absorbing particles in snow across the Arctic, North America, and China: Effects on surface albedo. *Journal of Geophysical Research: Atmospheres*, 122, 10,149–10,168. <https://doi.org/10.1002/2017JD027070>
- Dang, C., Zender, C. S., and Flanner, M. G. (2019). Inter-comparison and improvement of 2-stream shortwave radiative transfer models for unified treatment of cryospheric surfaces in ESMs, *The Cryosphere Discuss.*, <https://doi.org/10.5194/tc-2019-22>.
- Emmons, L. K., Walters, S., Hess, P. G., Lamarque, J. F., Pfister, G. G., Fillmore, D., Granier, C., Guenther, A., Kinnison, D., Laepple, T., Orlando, J., Tie, X., Tyndall, G., Wiedinmyer, C., Baughcum, S. L., & Kloster, S. (2010). Description and evaluation of the model for ozone and related chemical tracers, version 4 (MOZART-4). *Geoscientific Model Development*, 3(1), 43–67. <https://doi.org/10.5194/gmd-3-43-2010>
- Fanourgakis, G. S., Kanakidou, M., Nenes, A., Bauer, S. E., Bergman, T., Carslaw, et al., (2019), Evaluation of global simulations of aerosol particle and cloud condensation nuclei number, with implications for cloud droplet formation, *Atmos. Chem. Phys.*, 19, 8591–8617, <https://doi.org/10.5194/acp-19-8591-2019>.

- Flanner, M. G., C. S. Zender, J. T. Randerson, and P. J. Rasch (2007), Present-day climate forcing and response from black carbon in snow, *J. Geophys. Res.*, 112(D11), 202, doi:10.1029/2006JD008003.
- Flanner, M. G., X. Liu, C. Zhou, J. E. Penner, and C. Jiao (2012), Enhanced solar energy absorption by internally-mixed black carbon in snow grains, *Atmos. Chem. Phys.*, 12, 4699–4721.
- Gelaro, R., McCarty, W., Suárez, M. J., Todling, R., Molod, A., Takacs, L., ... Zhao, B. (2017). The Modern-Era Retrospective Analysis for Research and Applications, Version 2 (MERRA-2). *Journal of Climate*, 30(14), 5419–5454. <https://doi.org/10.1175/JCLI-D-16-0758.1>
- Gettelman, A. (2015), Putting the clouds back in aerosol–cloud interactions, *Atmos. Chem. Phys.*, 15, 12397–12411, doi:10.5194/acp-15-12397-2015.
- Gettelman, A., & Morrison, H. (2015). Advanced two-moment bulk microphysics for global models. Part I: Off-line tests and comparison with other schemes. *Journal of Climate*, 28(3), 1268–1287. <https://doi.org/10.1175/Jcli-D-14-00102.1>
- Gettelman, A., Morrison, H., Santos, S., Bogenschutz, P., & Caldwell, P. M. (2015). Advanced two-moment bulk microphysics for global models. Part II: Global model solutions and aerosol–cloud interactions. *Journal of Climate*, 28(3), 1288–1307. <https://doi.org/10.1175/jcli-d-14-00103.1>
- Ghan, S. J. (2013), Technical note: Estimating aerosol effects on cloud radiative forcing, *Atmos. Chem. Phys.*, 13, 9971–9974, doi:10.5194/acp-13-9971-2013.
- Ghan, S., et al. (2016), Challenges in constraining anthropogenic aerosol effects on cloud radiative forcing using present-day spatiotemporal variability, *Proc. Natl. Acad. Sci. U.S.A.*, 113(21), 5804–5811.
- Golaz, J.-C., V. E. Larson, and W. R. Cotton (2002), A pdf-based model for boundary layer clouds: Part I. Method and model description, *J. Atmos. Sci.*, 59(24), 3540–3551.
- Golaz, J.-C., et al. (2019). The DOE E3SM coupled model version 1: Overview and evaluation at standard resolution. *Journal of Advances in Modeling Earth Systems*, 11. <https://doi.org/10.1029/2018MS001603>
- Harikumar R, Sampath S, and Sasi KV. (2009). An empirical model for the variation of rain drop size distribution with rain rate at a few locations in Southern India. *Advances in Space Research*, 43: 837–844.
- Hoesly, R. M., Smith, S. J., Feng, L., Klimont, Z., Janssens-Maenhout, G., Pitkanen, T., Seibert, J. J., Vu, L., Andres, R. J., Bolt, R. M., Bond, T. C., Dawidowski, L., Kholod, N., Kurokawa, J.-I., Li, M., Liu, L., Lu, Z., Moura, M. C. P., O'Rourke, P. R., & Zhang, Q. (2018). Historical (1750–2014) anthropogenic emissions of reactive gases and aerosols from the Community Emissions Data System (CEDS). *Geoscientific Model Development*, 11(1), 369–408. <https://doi.org/10.5194/gmd-11-369-2018>
- Intergovernmental Panel on Climate Change (IPCC) (2013), Climate Change 2013: The Physical Science Basis, in Contribution of Working Group I to the Fifth Assessment Report of the Intergovernmental Panel on Climate Change, edited by T. F. Stocker et al., Cambridge Univ. Press, Cambridge, U. K., and New York.

- Jimenez, J. L., et al. (2009), Evolution of organic aerosols in the atmosphere, *Science*, 326(5959), 1525–1529, doi:10.1126/science.1180353.
- Khairoutdinov, M., and Y. Kogan (2000), A new cloud physics parameterization in a large-eddy simulation model of marine stratocumulus, *Mon. Weather Rev.*, 128(1), 229–243.
- Kinne, S., O'Donnel, D., Stier, P., Kloster, S., Zhang, K., Schmidt, H., Rast, S., Giorgetta, M., Eck, T. F., and Stevens, B. (2013). MAC-v1: A new global aerosol climatology for climate studies. *Journal of Advances in Modeling Earth Systems*, 5, 704–740. <https://doi.org/10.1002/jame.20035>
- Kokkola, H., R. Hommel, J. Kazil, U. Niemeier, A.-I. Partanen, J. Feichter, and C. Timmreck (2009), Aerosol microphysics modules in the framework of the ECHAM5 climate model—Intercomparison under stratospheric conditions, *Geosci. Model Dev.*, 2, 97–112, doi:10.5194/gmd-2-97-2009.
- Kopacz, M., D. L. Mauzerall, J. Wang, E. M. Leibensperger, D. K. Henze, and K. Singh (2011), Origin and radiative forcing of black carbon transported to the Himalayas and Tibetan Plateau, *Atmos. Chem. Phys.*, 11, 2837–2852, doi:10.5194/acp-11-2837-2011.
- Larson, V. E., Golaz, J.-C., & Cotton, W. R. (2002). Small-scale and mesoscale variability in cloudy boundary layers: Joint probability density functions. *Journal of the Atmospheric Sciences*, 59(24), 3519–3539. [https://doi.org/10.1175/1520-0469\(2002\)059<3519:SSAMVI>2.0.CO;2](https://doi.org/10.1175/1520-0469(2002)059<3519:SSAMVI>2.0.CO;2)
- Liu, X., Easter, R. C., Ghan, S. J., Zaveri, R., Rasch, P., Shi, X., Lamarque, J.-F., Gettelman, A., Morrison, H., Vitt, F., Conley, A., Park, S., Neale, R., Hannay, C., Ekman, A. M. L., Hess, P., Mahowald, N., Collins, W., Iacono, M. J., Bretherton, C. S., Flanner, M. G., & Mitchell, D. (2012). Toward a minimal representation of aerosols in climate models: Description and evaluation in the Community Atmosphere Model CAM5. *Geoscientific Model Development*, 5(3), 709–739. <https://doi.org/10.5194/gmd-5-709-2012>
- Liu, X., Ma, P. L., Wang, H., Tilmes, S., Singh, B., Easter, R. C., Ghan, S. J., & Rasch, P. J. (2016). Description and evaluation of a new four-mode version of the modal aerosol module (MAM4) within version 5.3 of the Community Atmosphere Model. *Geoscientific Model Development*, 9(2), 505–522. <https://doi.org/10.5194/gmd-9-505-2016>
- Mann, G. W., et al. (2014), Intercomparison and evaluation of global aerosol microphysical properties among AeroCom models of a range of complexity, *Atmos. Chem. Phys.*, 14, 4679–4713, doi:10.5194/acp-14-4679-2014.
- Mitra, S.K., J. Brinkmann, and H.R. Pruppacher (1992), A wind tunnel study on the drop-to-particle conversion. *J. Aerosol. Sci.*, 23, 245–256. [https://doi.org/10.1016/0021-8502\(92\)90326-Q](https://doi.org/10.1016/0021-8502(92)90326-Q)
- Morrison, H., and A. Gettelman (2008): A new two-moment bulk stratiform cloud microphysics scheme in the NCAR Community Atmosphere Model (CAM3). Part I: Description and numerical tests. *J. Climate*, 21, 3642–3659, doi:<https://doi.org/10.1175/2008JCLI2105.1>.
- Qian, Y., W. I. Gustafson Jr., L. R. Leung, and S. J. Ghan (2009), Effects of soot-induced snow albedo change on snowpack and hydrological cycle in western United States based on Weather Research and Forecasting chemistry and regional climate simulations, *J. Geophys. Res.*, 114, D03108, doi:10.1029/2008JD011039.

- Qian, Y., M. Flanner, L. Leung, and W. Wang (2011), Sensitivity studies on the impacts of Tibetan Plateau snowpack pollution on the Asian hydrological cycle and monsoon climate, *Atmos. Chem. Phys.*, 11(5), 1929–1948, doi:10.5194/acp-11-1929-2011.
- Qian, Y., H. Wang, R. Zhang, M. G. Flanner, and P. J. Rasch (2014), A sensitivity study on modeling black carbon in snow and its radiative forcing over the Arctic and Northern China, *Environ. Res. Lett.*, 9, 064001, doi:10.1088/1748-9326/9/6/064001.
- Qian, Y., T. J. Yasunari, S. J. Doherty, M. G. Flanner, W. K. M. Lau, J. Ming, H. Wang, M. Wang, S. G. Warren, and R. Zhang (2015), Light-absorbing particles in snow and ice: Measurement and modeling of climatic and hydrological impact, *Adv. Atmos. Sci.*, 32(1), 64–91, doi:10.1007/s00376-014-0010-0.
- Rahimi, S., X. Liu, C. Wu, W. K. Lau, H. Brown, M. Wu, and Y. Qian (2019), Quantifying snow darkening and atmospheric radiative effects of black carbon and dust on the South Asian monsoon and hydrological cycle: experiments using variable-resolution CESM, *Atmos. Chem. Phys.*, 19, 12025–12049, <https://doi.org/10.5194/acp-19-12025-2019>.
- Rasch, P. J., et al. (2019). An overview of the atmospheric component of the Energy Exascale Earth System Model. *Journal of Advances in Modeling Earth Systems*, 11, 2377–2411. doi:<https://doi.org/10.1029/2019MS001629>.
- Rogers, R. R., and M. K. Yau (1989), A short course in cloud physics, Pergamon, New York, 293 pp.
- Rosenfeld, D., et al. (2014), Global observations of aerosol-cloud-precipitation-climate interactions, *Rev. Geophys.*, 52, 750–808, doi:[10.1002/2013RG000441](https://doi.org/10.1002/2013RG000441).
- Shilling, J. E., et al. (2009), Loading-dependent elemental composition of alpha-pinene SOA particles, *Atmos. Chem. Phys.*, 9(3), 771–782.
- Shrivastava, M., Easter, R. C., Liu, X., Zelenyuk, A., Singh, B., Zhang, K., Ma, P.-L., Chand, D., Ghan, S., Jimenez, J. L., Zhang, Q., Fast, J., Rasch, P. J., & Tiitta, P. (2015). Global transformation and fate of SOA: Implications of low-volatility SOA and gas-phase fragmentation reactions. *Journal of Geophysical Research: Atmospheres*, 120, 4169–4195. <https://doi.org/10.1002/2014JD022563>
- Slinn, W. G. N. (1984) Precipitation scavenging, Atmospheric Science and Power Production D. Randerson, 466–532, U.S. Department of Energy, Technical Information Center, Oak Ridge, Tenn.
- Sorooshian, A., B. Anderson, S.E. Bauer, R.A. Braun, B. Cairns, E. Crosbie, et al., (2019), Aerosol–Cloud–Meteorology Interaction Airborne Field Investigations: Using Lessons Learned from the U.S. West Coast in the Design of ACTIVATE off the U.S. East Coast. *Bull. Amer. Meteor. Soc.*, 100, 1511–1528, <https://doi.org/10.1175/BAMS-D-18-0100.1>
- Turpin, B. J., and H. J. Lim (2001), Species contributions to PM_{2.5} mass concentrations: Revisiting common assumptions for estimating organic mass, *Aerosol Sci. Technol.*, 35(1), 602–610, doi:10.1080/02786820152051454.
- van Marle, M. J. E., Kloster, S., Magi, B. I., Marlon, J. R., Daniau, A.-L., Field, R. D., et al. (2017). Historic global biomass burning emissions for CMIP6 (BB4CMIP) based on merging satellite observations with proxies and fire models (1750–2015). *Geoscientific Model Development*, 10(9), 3329–3357. <https://doi.org/10.5194/gmd-10-3329-2017>

- Wan, H., Rasch, P. J., Zhang, K., Kazil, J., & Leung, L. (2013). Numerical issues associated with compensating and competing processes in climate models: An example from ECHAM-HAM. *Geoscientific Model Development*, 6(3), 861–874.
- Wang, H., Easter, R. C., Rasch, P. J., Wang, M., Liu, X., Ghan, S. J., et al. (2013). Sensitivity of remote aerosol distributions to representation of cloud-aerosol interactions in a global climate model. *Geoscientific Model Development*, 6(3), 765–782.
<https://doi.org/10.5194/gmd-6-765-2013>
- Wang, H., P. J. Rasch, and G. Feingold (2011), Manipulating marine stratocumulus cloud amount and albedo: A process-modelling study of aerosol-cloud-precipitation interactions in response to injection of cloud condensation nuclei, *Atmos. Chem. Phys.*, 11, 4237–4249, doi:10.5194/acp-11-4237-2011.
- Wang, H., Rasch, P. J., Easter, R. C., Singh, B., Zhang, R., Ma, P. L., et al. (2014). Using an explicit emission tagging method in global modeling of source-receptor relationships for black carbon in the Arctic: Variations, sources, and transport pathways. *Journal of Geophysical Research: Atmospheres*, 119, 12,888–12,909.
<https://doi.org/10.1002/2014JD022297>
- Wang, M., et al. (2012), Constraining cloud lifetime effects of aerosols using A-Train satellite observations, *Geophys. Res. Lett.*, 39, L15709, doi:10.1029/2012GL052204.
- Wang, Y., Liu, X., Hoose, C., & Wang, B. (2014). Different contact angle distributions for heterogeneous ice nucleation in the Community Atmospheric Model version 5. *Atmospheric Chemistry and Physics*, 14(19), 10,411–10,430. <https://doi.org/10.5194/acp-14-10411-2014>
- Warren, S. G., and W. J. Wiscombe (1980), A model for the spectral albedo of snow. II: Snow containing atmospheric aerosols, *J. Atmos. Sci.*, 37(12), 2734–2745.
- Wu, C., X. Liu, Z. Lin, S.R., Rahimi-Esfarjani, Z. Lu (2018), Impacts of absorbing aerosol deposition on snowpack and hydrologic cycle in the Rocky Mountain region based on variable-resolution CESM (VR-CESM) simulations. *Atmos. Chem. Phys.*, 18, 511–533, <https://doi.org/10.5194/acp-18-511-2018>.
- Xie, S., et al. (2018). Understanding cloud and convective characteristics in version 1 of the E3SM Atmosphere Model. *Journal of Advances in Modeling Earth Systems*, 10, 2618–2644. <https://doi.org/10.1029/2018ms001350>
- Yang, Y., Wang, H., Smith, S. J., Zhang, R., Lou, S., Qian, Y., Ma, P.-L., & Rasch, P. J. (2018a). Recent intensification of winter haze in China linked to foreign emissions and meteorology. *Scientific Reports*, 8(1), 2107. <https://doi.org/10.1038/s41598-018-20437-7>
- Yang, Y., Wang, H., Smith, S. J., Zhang, R., Lou, S., Yu, H., Li, C., & Rasch, P. J. (2018b). Source apportionments of aerosols and their direct radiative forcing and long-term trends over continental United States. *Earth's Future*, 6(6), 793–808.
<https://doi.org/10.1029/2018EF000859>
- Yu, F., and G. Luo (2009), Simulation of particle size distribution with a global aerosol model: Contribution of nucleation to aerosol and CCN number concentrations, *Atmos. Chem. Phys.*, 9(20), 7691–7710.

- Zhang, K., et al. (2018). Impact of numerical choices on water conservation in the E3SM Atmosphere Model version 1 (EAMv1). *Geoscientific Model Development*, 11(5), 1971–1988. <https://doi.org/10.5194/gmd-11-1971-2018>
- Zhang, L. M., Gong, S. L., Padro, J., & Barrie, L. (2001). A size-segregated particle dry deposition scheme for an atmospheric aerosol module, *Atmos. Environment*, 35(3), 549–560. [https://doi.org/10.1016/s1352-2310\(00\)00326-5](https://doi.org/10.1016/s1352-2310(00)00326-5)
- Zhang, Q., et al. (2007). Ubiquity and dominance of oxygenated species in organic aerosols in anthropogenically-influenced Northern Hemisphere midlatitudes, *Geophys. Res. Lett.*, 34, L13801, doi:10.1029/2007gl029979.
- Zhang, R., D. A. Hegg, J. Huang, and Q. Fu (2013), Source attribution of insoluble light-absorbing particles in seasonal snow across northern China, *Atmos. Chem. Phys.*, 13(12), 6091–6099.
- Zhang, R., H. Wang, D. A. Hegg, Y. Qian, S. J. Doherty, C. Dang, P. L. Ma, P. J. Rasch, and Q. Fu (2015), Quantifying sources of black carbon in western North America using observationally based analysis and an emission tagging technique in the Community Atmosphere Model, *Atmos. Chem. Phys.*, 15, 12,805–12,822, doi:10.5194/acp-15-12805-2015.
- Zhang, S., et al. (2016). On the characteristics of aerosol indirect effect based on dynamic regimes in global climate models. *Atmospheric Chemistry and Physics*, 16(5), 2765–2783. <https://doi.org/10.5194/acp-16-2765-2016>

Table 1. Short simulations designed to examine the impact of individual aerosol-related new changes on global aerosols and radiative forcing in the EAMv1 framework. Wind fields are nudged to MERRA-2 reanalysis. The empty box in each column indicates that the corresponding new treatment is excluded in the simulation.

Simulation Design (CTRL has all the new treatments and others have all but one of the new treatments)	Aerosol process treatment						
	New treatment of H ₂ SO ₄ vapor for new particle formation (NewH2SO4)	New treatment of convective transport and aerosol wet removal (NewConvTran)	New treatment of SOA (NewSOA)	New treatment of MOA (NewMOA)	New ice-nucleation treatment (NewIceNuc)	New resuspension of aerosols from evaporating precipitation (NewResusp)	New treatment of LAPs in snow and ice at the surface (NewInSnow)
CTRL	x	x	x	x	x	x	x
noNewH2SO4		x	x	x	x	x	x
noNewConvTran	x		x	x	x	x	x
noNewSOA	x	x		x	x	x	x
noNewMOA	x	x	x		x	x	x
noNewIceNuc	x	x	x	x		x	x
noNewResusp	x	x	x	x	x		x
noNewInSnow	x	x	x	x	x	x	

Table 2. Impact of the NewResusp treatment on global averages of several aerosol, cloud, and radiative parameters. Results are shown for EAMv1 (V1) and EAMv0 (V0) simulations with the new-nonlinear, new-linear, and old rain-evaporation resuspension treatment simulations. Results for the new-linear and old resuspension-treatment simulations are shown as relative differences (%) from the corresponding new-nonlinear resuspension-treatment simulation that uses units in the first column. CCN and particle number concentration in the four modes are tropospheric mean.

	V1 new-nonlinear resuspension	V1 new-linear resuspension	V1 old resuspension	V0 new-nonlinear resuspension	V0 new-linear resuspension	V0 old resuspension
Sulfate burden (Tg S)	0.660	2.4%	5.3%	0.575	5.6%	25.0%
BC burden (Tg)	0.160	1.3%	4.5%	0.126	2.7%	21.7%
POM burden (Tg)	0.926	1.3%	4.5%	0.983	2.6%	19.1%
SOA burden (Tg)	2.82	2.6%	4.9%	1.06	6.4%	28.5%
Dust burden (Tg)	14.9	1.9%	3.4%	25.9	6.6%	17.5%
Sea salt burden (Tg)	4.65	2.6%	7.2%	11.3	4.3%	14.4%
AOD	0.132	0.8%	8.5%	0.123	1.8%	32.9%
AAOD	0.00799	1.4%	4.7%	0.00749	3.8%	23.8%
Accumulation mode number (mg^{-1})	180	0.1%	1.9%	103	0.3%	19.1%
Primary carbon mode number (mg^{-1})	29.7	-0.6%	2.0%	51.7	-1.3%	11.2%
Aitken mode number (mg^{-1})	485	-0.5%	-6.6%	164	-1.1%	-18.8%
Coarse mode number (mg^{-1})	0.231	0.3%	7.9%	0.312	0.5%	37.6%
CCN at 0.1% S (mg^{-1})	38.5	0.3%	7.3%	27.4	0.3%	37.5%
CCN at 0.1% S (sfc to 700 hPa) (mg^{-1})	65.1	0.2%	9.2%	55.5	0.1%	35.9%
Cloud droplet number column burden (10^9 m^{-2})	14.1	0.0%	7.3%	12.6	-0.1%	36.3%
Cloud liquid water path (g m^{-2})	49.2	0.0%	0.8%	45.8	-0.2%	11.3%
Short-wave cloud forcing (W m^{-2})	-44.6	0.0%	0.6%	-54.6	-0.4%	3.5%
Long-wave cloud forcing (W m^{-2})	22.3	0.0%	-0.2%	25.9	-0.2%	-0.3%

Table 3. Global-average annual precipitation production rate, precipitation rate, precipitation fractional contribution, and evaporation/production for deep convection, shallow convection, and stratiform clouds. In the EAMv1 (referred to as V1) model, stratiform and shallow convective clouds are treated together. Results are from the CTRL (for V1) and EAMv0 (referred to as V0) simulations with the new nonlinear resuspension treatment.

	Column precip. production (mm/yr)	Column evaporation/ production (%)	Surface precipitation (mm/yr)	Fractional precip. contribution (%)
V1 Deep Convective	712.9	8.4	653.0	58.5
V1 Stratiform + Shallow	613.5	24.5	463.5	41.5
V0 Deep Convective	669.3	5.0	635.8	59.5
V0 Stratiform + Shallow	838.2	48.5	432.0	40.5
V0 Stratiform	706.6	55.2	316.5	29.6
V0 Shallow Convective	131.6	12.2	115.5	10.8

Table 4. Global annual average wet removal and resuspension fractions (as percentages) for aerosol species by cloud/precipitation type. The wet removal values are $100 \times (\text{cloud-type wet removal}) / (\text{total wet + dry removal})$. The resuspension values are $100 \times (\text{cloud-type resuspension}) / (\text{cloud-type scavenging})$. Wet removal here is the net wet removal; it is equal to scavenging minus resuspension aerosol transfer rates. The scavenging transfer is that from in-cloud and below-cloud scavenging processes, i.e., the transfer of interstitial and cloudborne aerosol to precipitation-borne aerosol. The resuspension transfer is the transfer of precipitation-borne aerosol back to interstitial aerosol. Results are from the new-nonlinear resuspension-treatment simulations.

	V1 Stratiform + Shallow	V0 Stratiform + Shallow	V1 Deep Convective	V0 Deep Convective
Wet Removal Fractions				
SO ₄	48.3	56.7	34.7	25.7
BC	27.8	45.7	35.1	28.6
POM	28.4	43.5	39.1	31.4
SOA	53.3	43.3	36.1	41.3
Sea Salt	12.7	30.1	20.0	19.4
Dust	10.8	20.2	12.1	14.5
Resuspension Fractions				
SO ₄	9.8	39.6	0.4	0.1
BC	10.6	41.7	0.4	0.1
POM	11.6	44.9	0.4	0.1
SOA	13.1	44.1	0.4	0.1
Sea Salt	9.6	23.1	0.1	0.0
Dust	8.1	53.8	1.0	0.4

Table A1. Coefficients for 9th-order fitted polynomials for ϕ_A and ϕ_N for the Marshall-Palmer and lognormal raindrop size distributions (a₁-a₉), and for the linear fit used for small values of f_{EV-W} (b₁-b₂).

	ϕ_A Marshall-Palmer	ϕ_A Lognormal	ϕ_N Marshall-Palmer	ϕ_N Lognormal
a1	8.6591133737322856E-02	6.1944215103685640E-02	4.5461070198414655E+00	-5.2335291116884175E-02
a2	- 1.7389168499601941E+00	- 2.0095166685965378E+00	- 3.0381753620077529E+01	2.7203158069178226E+00
a3	2.7401882373663732E+01	2.3882460251821236E+01	1.7959619926085665E+02	9.4730878152409375E+00
a4	- 1.5861714653209464E+02	- 1.2695611774753374E+02	- 6.7152282193785618E+02	5.0573187592544798E+01
a5	5.1338179363011193E+02	4.0086943562320101E+02	1.5651931323557126E+03	9.4732631441282862E+01
a6	- 9.6835933124501412E+02	- 7.4954272875943707E+02	- 2.2743927701175126E+03	8.8265926556465814E+01
a7	1.0588489932213311E+03	8.1701055892023624E+02	2.0004645897056735E+03	3.5247835268269142E+01
a8	- 6.2184513459217271E+02	- 4.7941894659538502E+02	- 9.7351466279626209E+02	1.5404586576716444E+00
a9	1.5184126886039758E+02	1.1710291076059025E+02	2.0101198012962413E+02	- 3.8228795492549068E+00
b1	5.0000000000000003E-02	1.0000000000000001E-01	5.0000000000000003E-02	1.0000000000000001E-01
b2	2.5622471203221014E-03	6.2227889828044350E-04	1.7005858490684875E-01	2.7247994766566485E-02

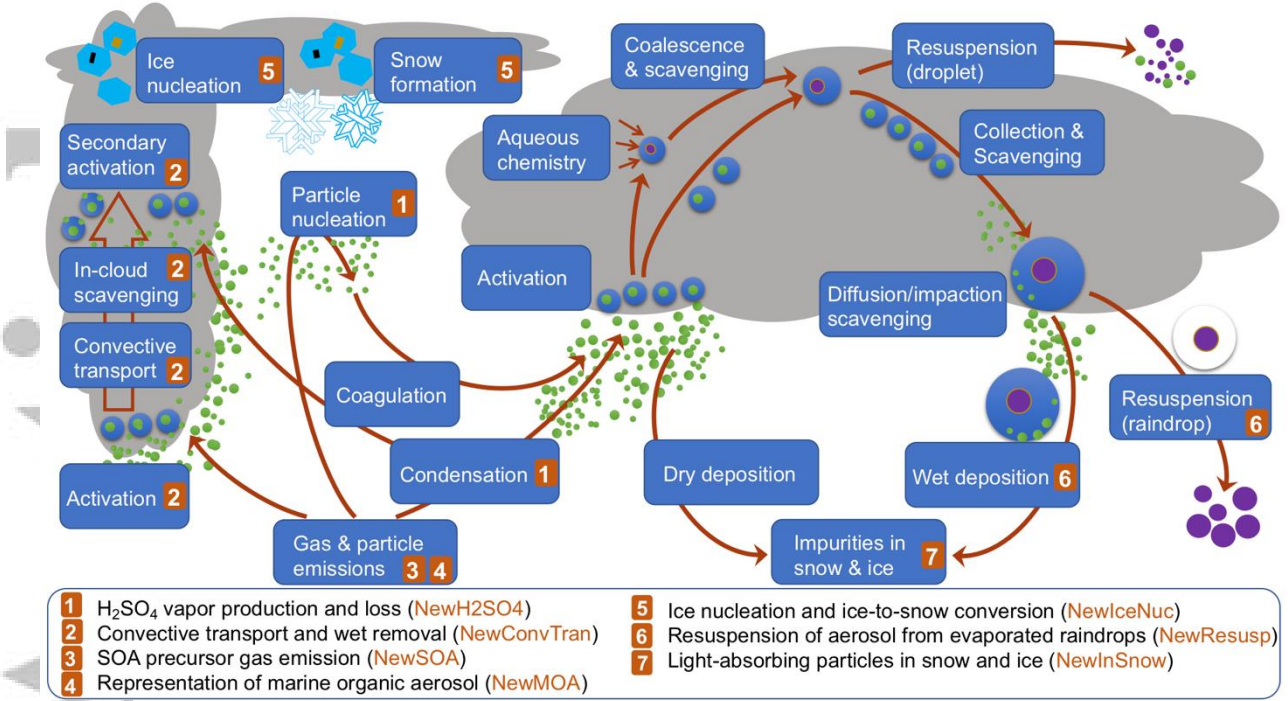


Figure 1: Schematic diagram of aerosol-related processes, denoted by blue boxes in clear air, stratiform cloud (shaded area on the right), convective cloud (shaded area on the left), or ice cloud (shaded area on the upper left) in E3SMv1. Compared to E3SMv0, there are newly added processes (i.e., cloud-base activation and secondary activation in convective cloud; resuspension of aerosols to the coarse mode; aerosol linked to ice nucleation) or old ones that are affected by individual new treatments in E3SMv1. The new treatments are listed in the legend at the bottom and are marked on the processes that are directly modified or added, as detailed in Section 2. The aging process (i.e., primary-carbon mode particles transferred to accumulation mode through condensation and coagulation) is not explicitly depicted here. The diffusion/impaction scavenging process (i.e., capture of interstitial aerosol particles by precipitation particles through Brownian diffusion and inertial impaction, which occurs both in clear air and clouds) is referred to as below-cloud scavenging in previous MAM aerosol studies (e.g., Liu et al., 2012; Wang et al., 2013).

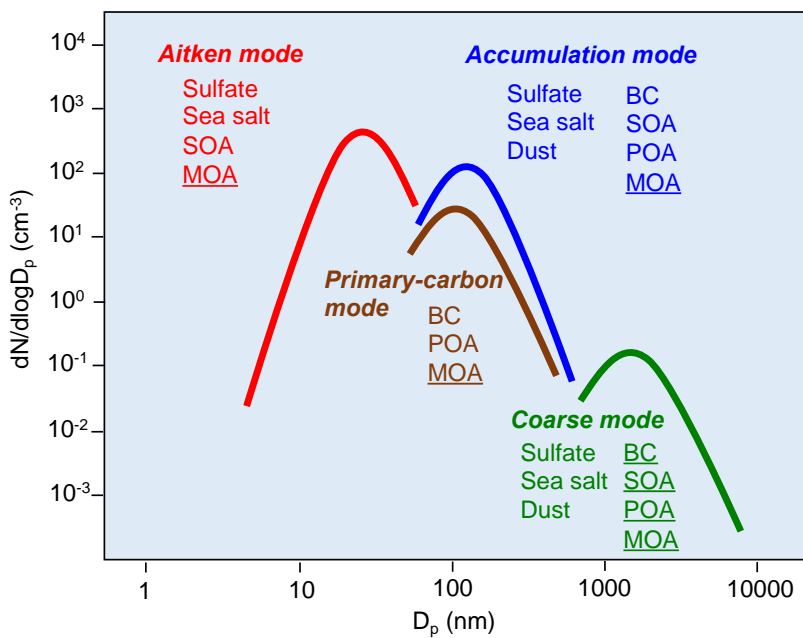


Figure 2: Schematic of the original and enhanced MAM4 aerosol representation. Combinations of aerosol species are treated in four size modes (Aitken, primary-carbon, accumulation and coarse mode), including the new marine organic aerosol (MOA) and all four carbonaceous aerosols (underlined) in the coarse mode for the enhanced MAM4.

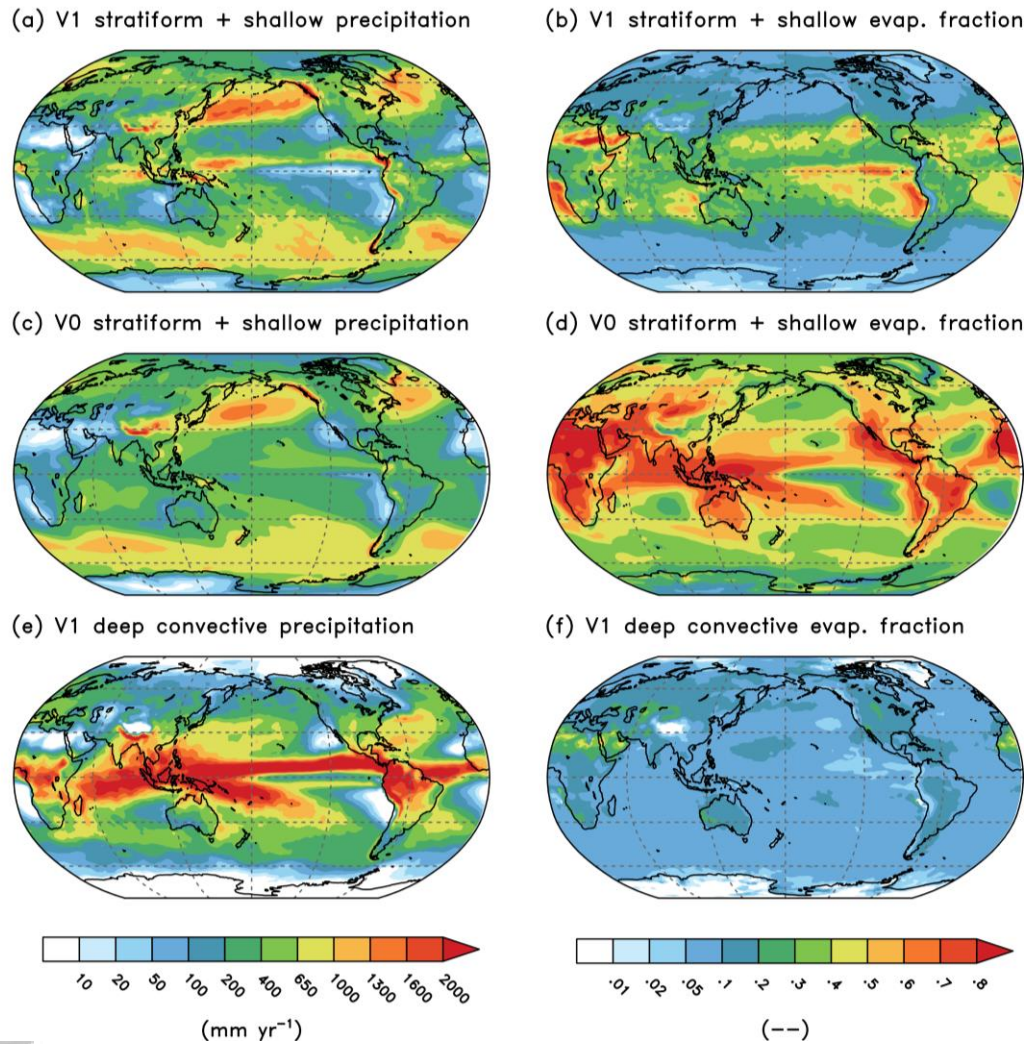


Figure 3: Horizontal distributions of annual-average surface precipitation rates (left panels) and column precipitation evaporation fractions (right panels) for V1-model stratiform + shallow convective precipitation, V0-model stratiform + shallow convective precipitation, and V1-model deep convective precipitation. The evaporation fraction is the column-integrated evaporation loss rate divided by the column precipitation production rate. Results are from the new-nonlinear resuspension treatment simulations.

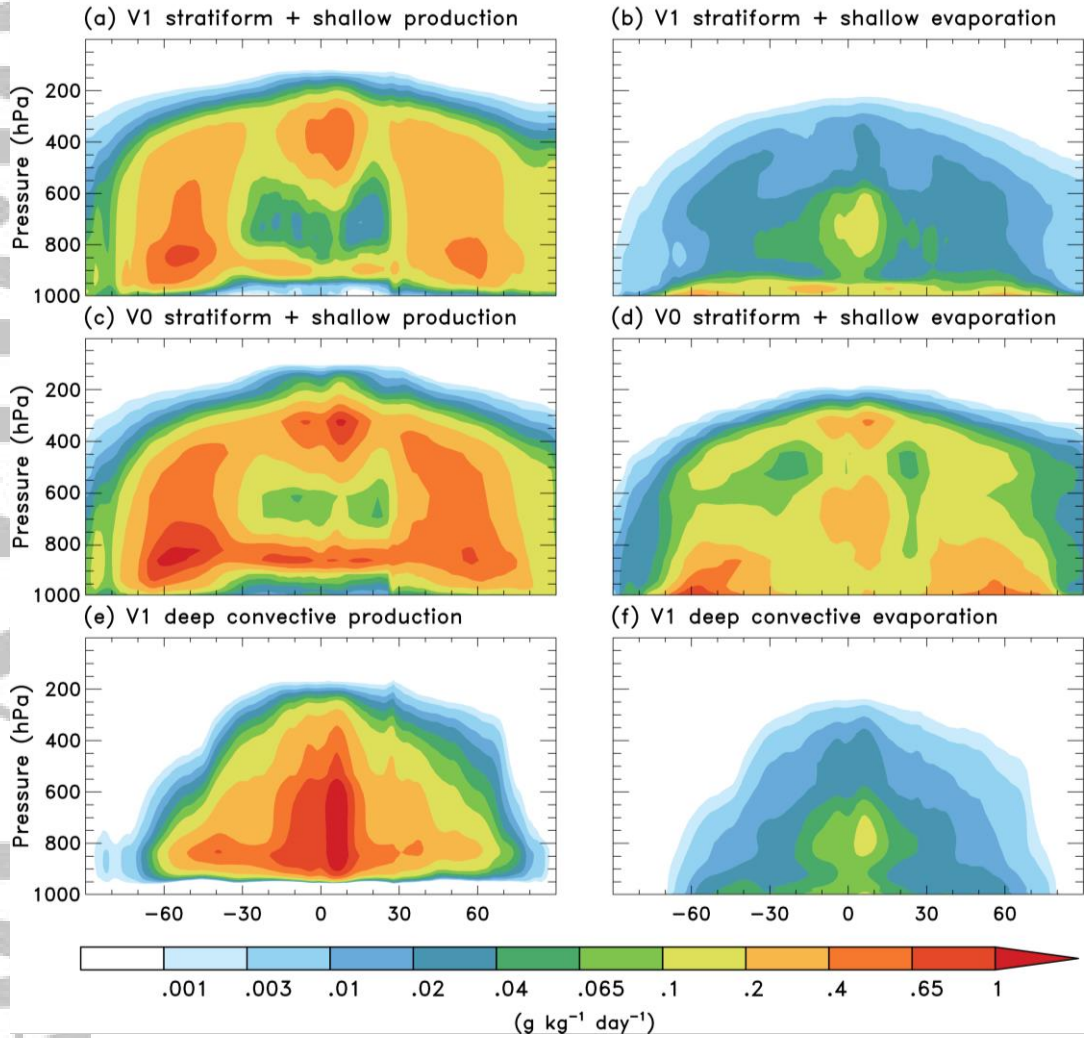


Figure 4: Zonal-average distributions of annual-average precipitation production rates (left panels) and precipitation evaporation rates (right panels) for V1-model stratiform + shallow convective precipitation, V0-model stratiform + shallow convective precipitation, and V1-model deep convective precipitation. Results are from the new-nonlinear resuspension treatment simulations.

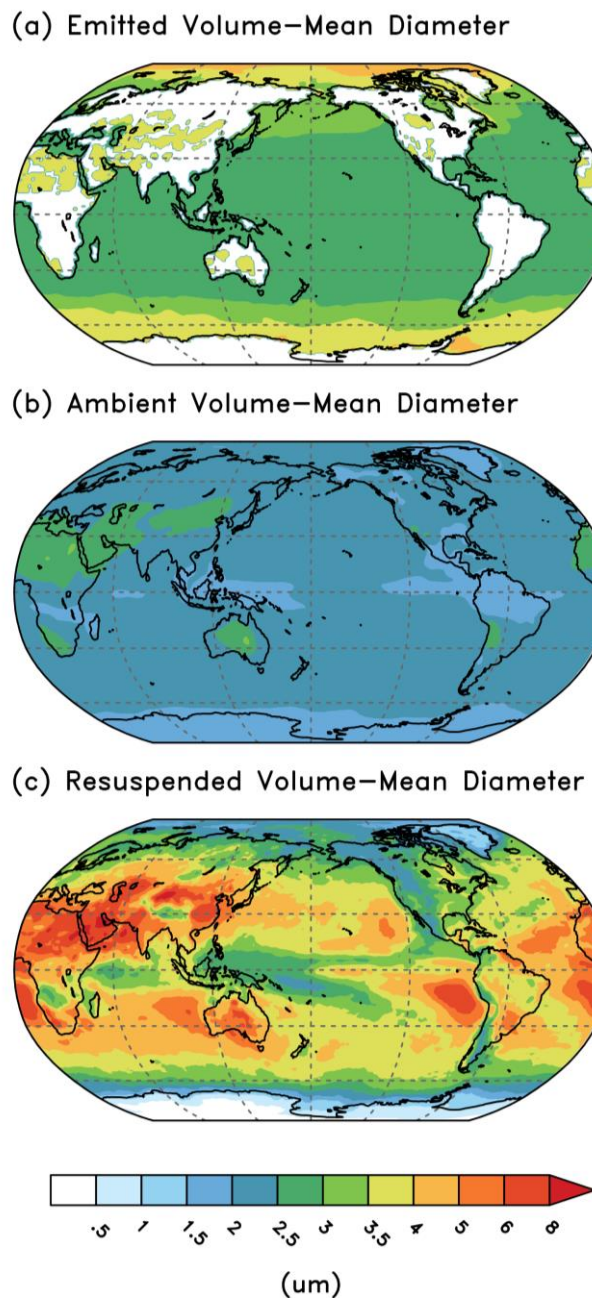


Figure 5: Horizontal distributions of annual- and vertical-average coarse-mode volume-mean diameters for (a) freshly emitted particles, (b) ambient particles, and (c) particles produced by resuspension from evaporating precipitation. Results are from the V1-model new-nonlinear resuspension treatment simulation, and vertical averages are for the troposphere.

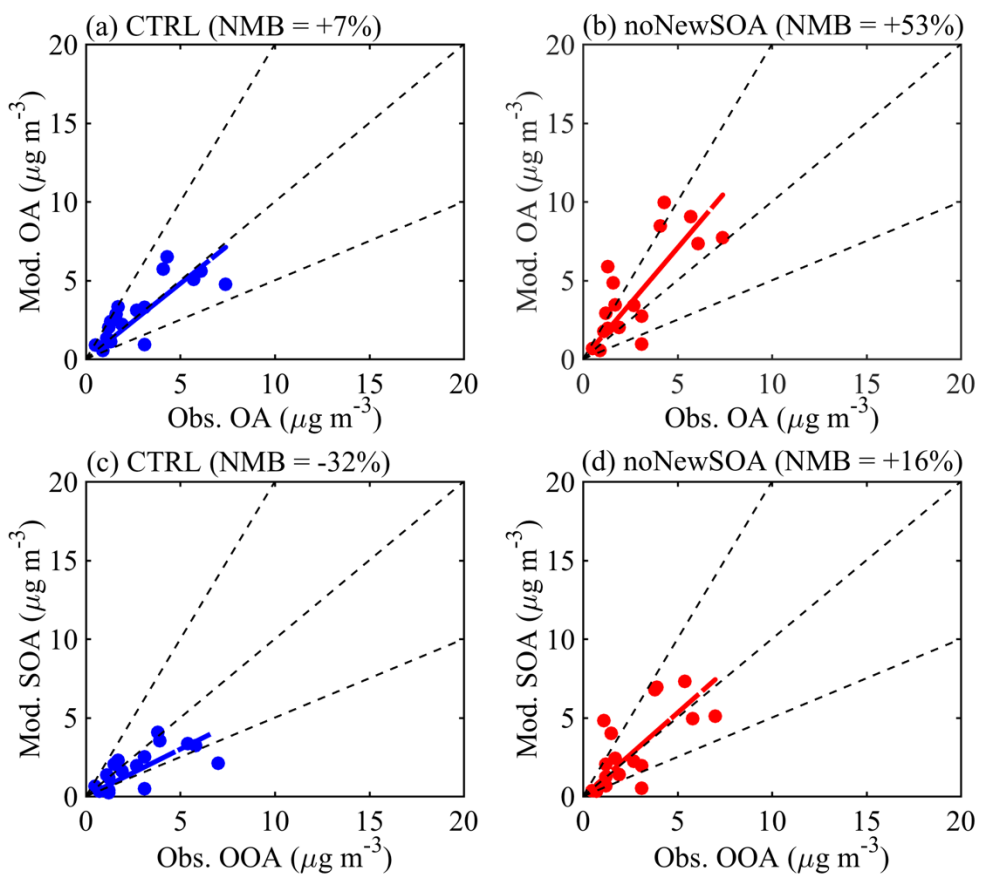


Figure 6: Scatterplots comparing simulated surface total OA (top panel) and SOA (bottom panel) concentrations from (a, c) CTRL, (b, d) noNewSOA simulations to observations at multiple sites over the globe. The observed total OA is the sum of hydrocarbon-like organic aerosol (HOA) and oxygenated organic aerosol (OOA) while the simulated OA includes POA and SOA. A total of 17 rural/remote site observations are used here (site location shown in Fig. S7). OOA is assumed to be the main contributor to SOA at these sites. The slope and coefficient R are obtained from the linear fit and correlation coefficient between simulated and measured OA or OOA concentrations. The dashed lines mark a 2:1, 1:1 and 1:2 ratios, respectively, between the simulated SOA and observed OOA.

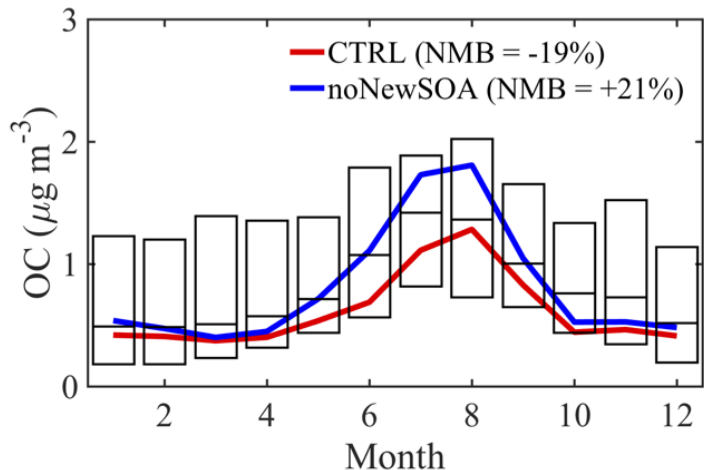


Figure 7: Observed and simulated monthly OC concentrations from 165 Interagency Monitoring of Protected Visual Environments (IMPROVE) sites in U.S. during 2007-2011. The boxes denote the observed median, the 15th and 85th percentiles. The colored lines correspond to median values of corresponding model simulated OC concentrations. Normalized mean biases (NMB), calculated throughout the year, are shown in numbers in the parentheses.

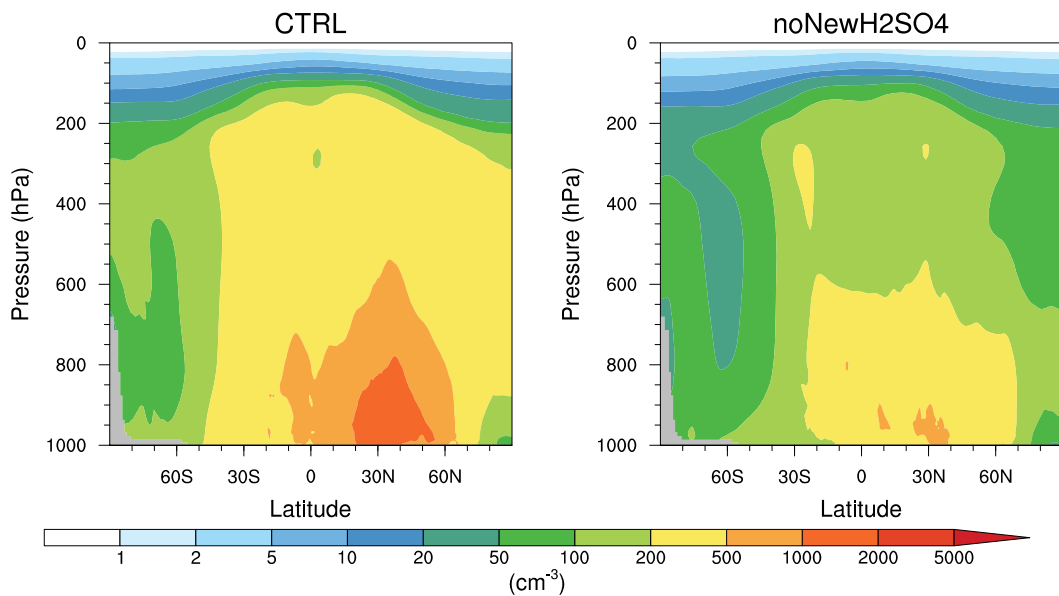


Figure 8: Vertical and meridional distributions of zonally averaged annual mean CN_{30} (defined as the number concentration of particles with diameter $D_p > 30 \text{ nm}$) simulated in CTRL and noNewH₂S_O₄.

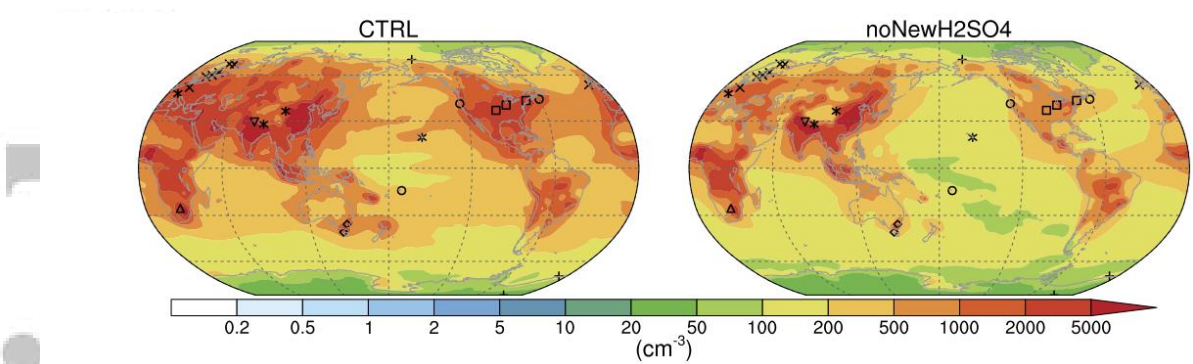


Figure 9: Global distribution of near-surface number concentration of CN_{30} ($D_p > 30 \text{ nm}$) for CTRL and noNewH₂S₄. Symbols mark the location of surface stations or high-elevation sites used in Figure 10.

Accepted

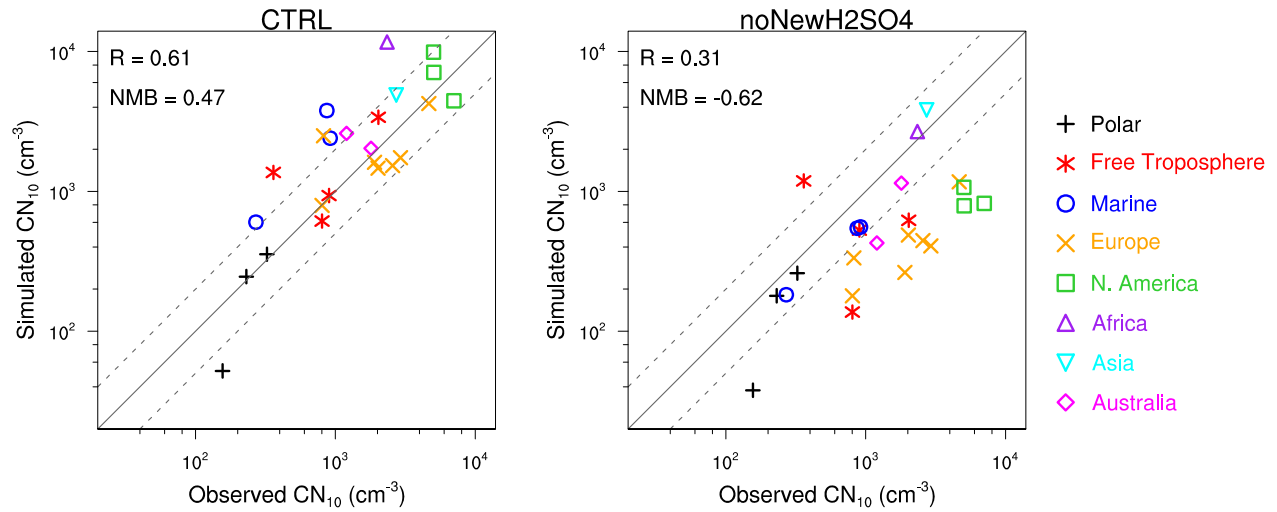


Figure 10: Comparison of model simulated CN_{10} (number concentration of particles with diameter $D_p > 10 \text{ nm}$) in CTRL and noNewH₂S_O₄ to the observed CN_{10} at various surface stations around the globe, among which four sites have high elevations (1-4 km), marked as “free troposphere”, as located in Figure 9. The solid line marks a 1:1 ratio, while the two dashed lines denote 2:1 and 1:2 ratios, respectively, between the simulated and observed CN_{10} .

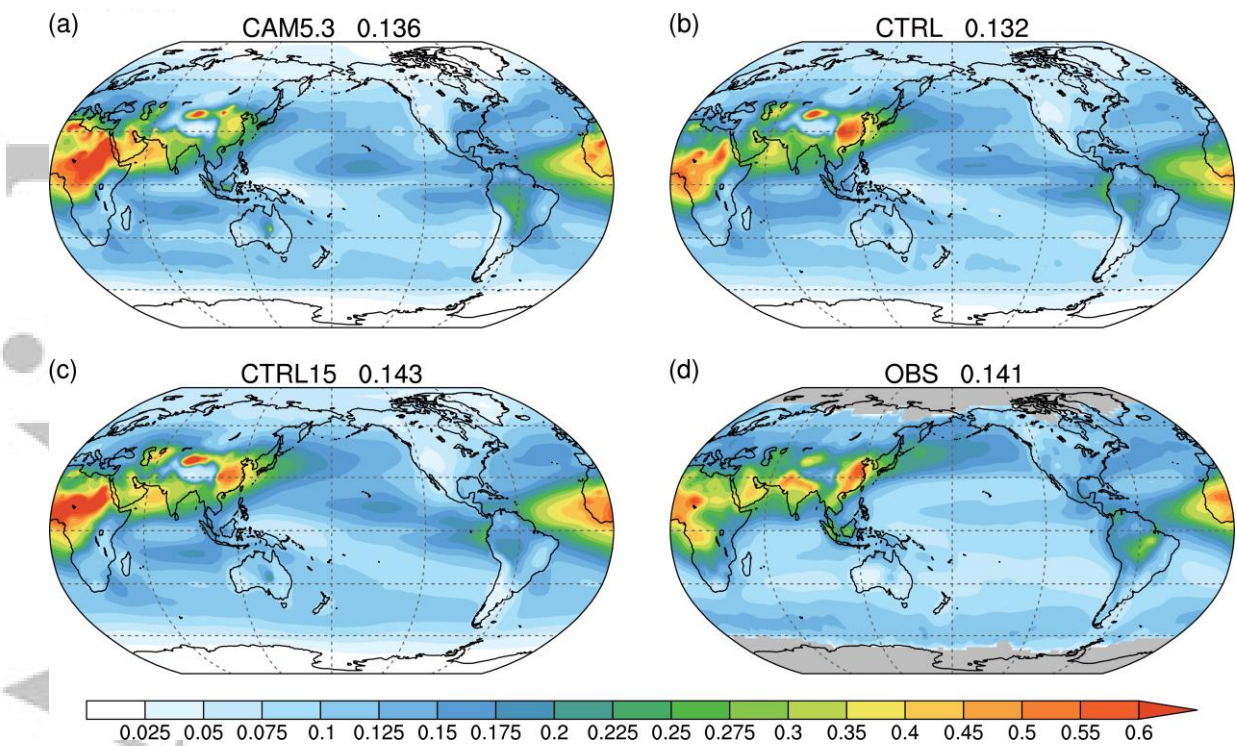


Figure 11: Global aerosol optical depth (AOD) from (a) CAM5.3, (b) CTRL (year 2007) and (c) CTRL15 (2000-2014), compared to (d) observational composite (OBS) with gray shading in polar regions indicating missing value. Numbers are the corresponding global mean.

Accepted Article

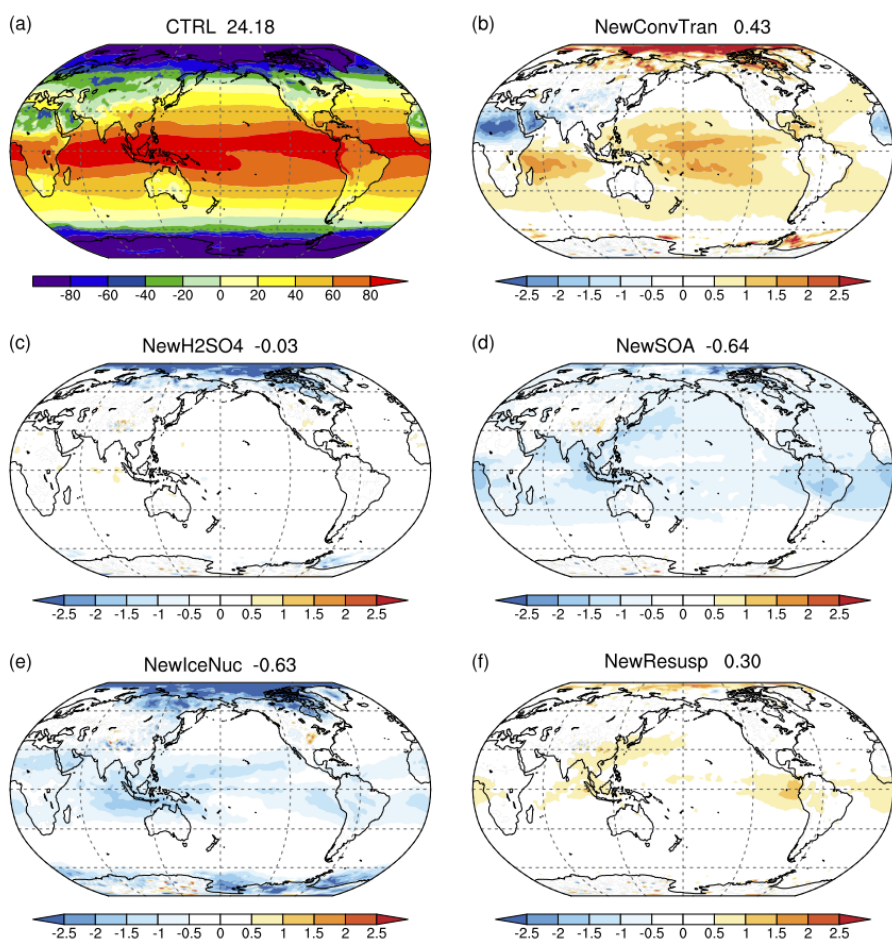


Figure 12: TOA clear-sky net radiative flux (W m^{-2}) under present-day (PD) aerosol conditions for (a) the CTRL simulation, and (b), (c), (d), (e) and (f) the difference between CTRL and five sensitivity simulations to show the effect of individual new treatment denoted by NewConvTran, NewH2SO4, NewSOA, NewIceNuc and NewInSnow (described in Table 1 and Fig. 1), respectively. The number on the top of each panel is the corresponding global mean value.

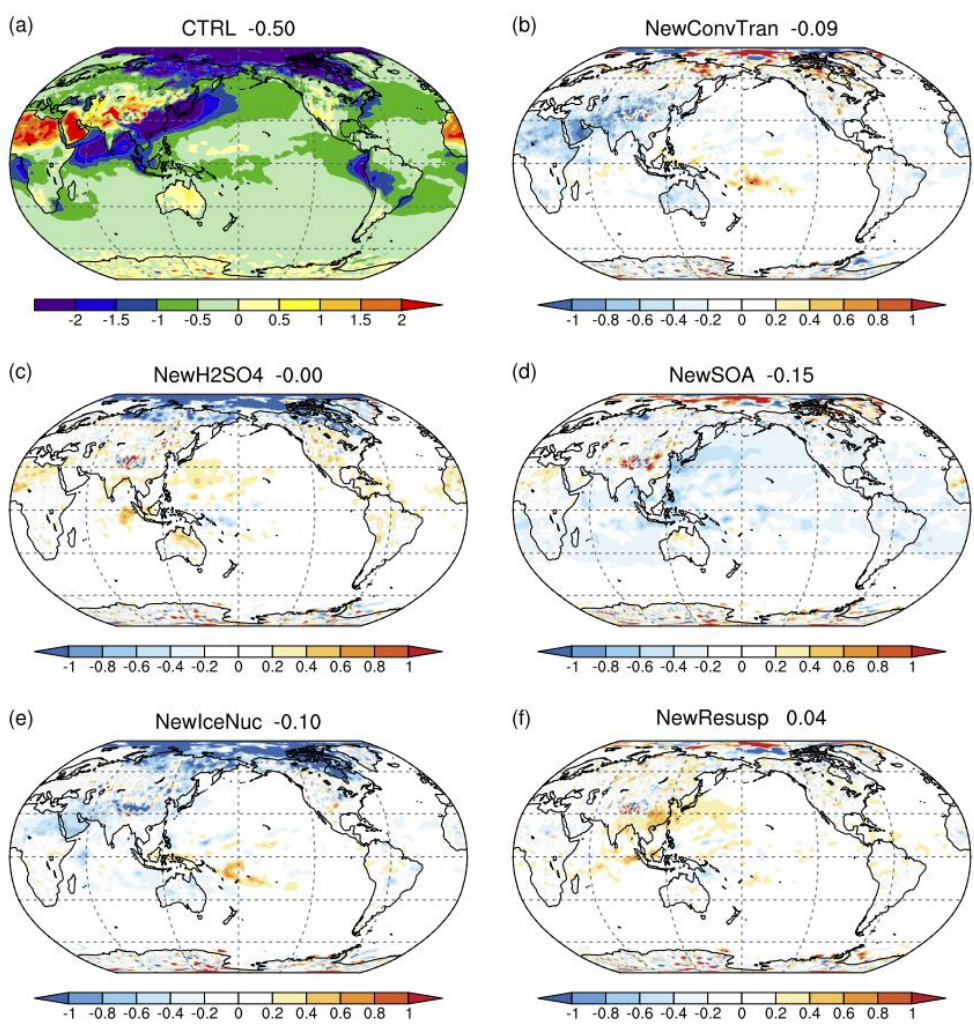


Figure 13: Same as Fig. 12 but for the difference in TOA clear-sky net radiative fluxes between two simulations with present-day (PD) and pre-industrial (PI) aerosol conditions, respectively.

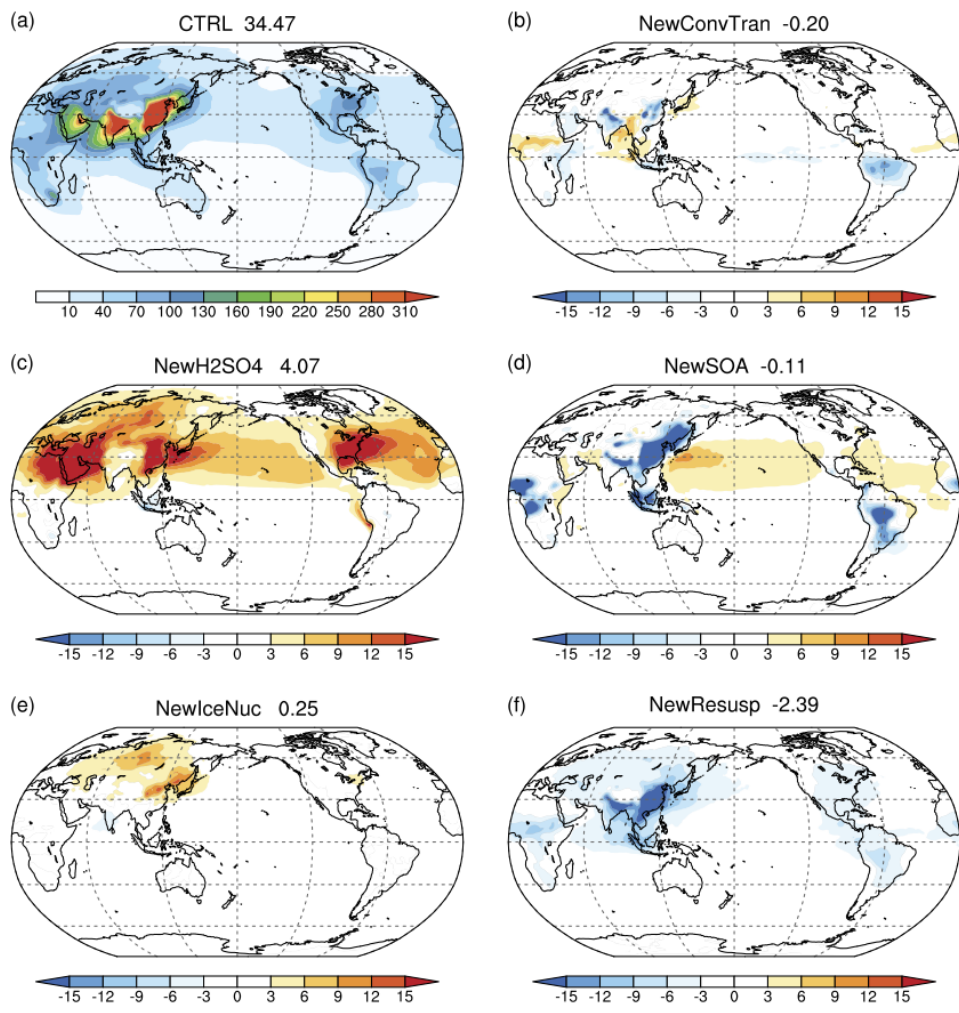


Figure 14: Same as Fig. 13 but for the column mean CCN concentration (cm^{-3}) at 0.1% supersaturation in the lower troposphere (below 850 mb).

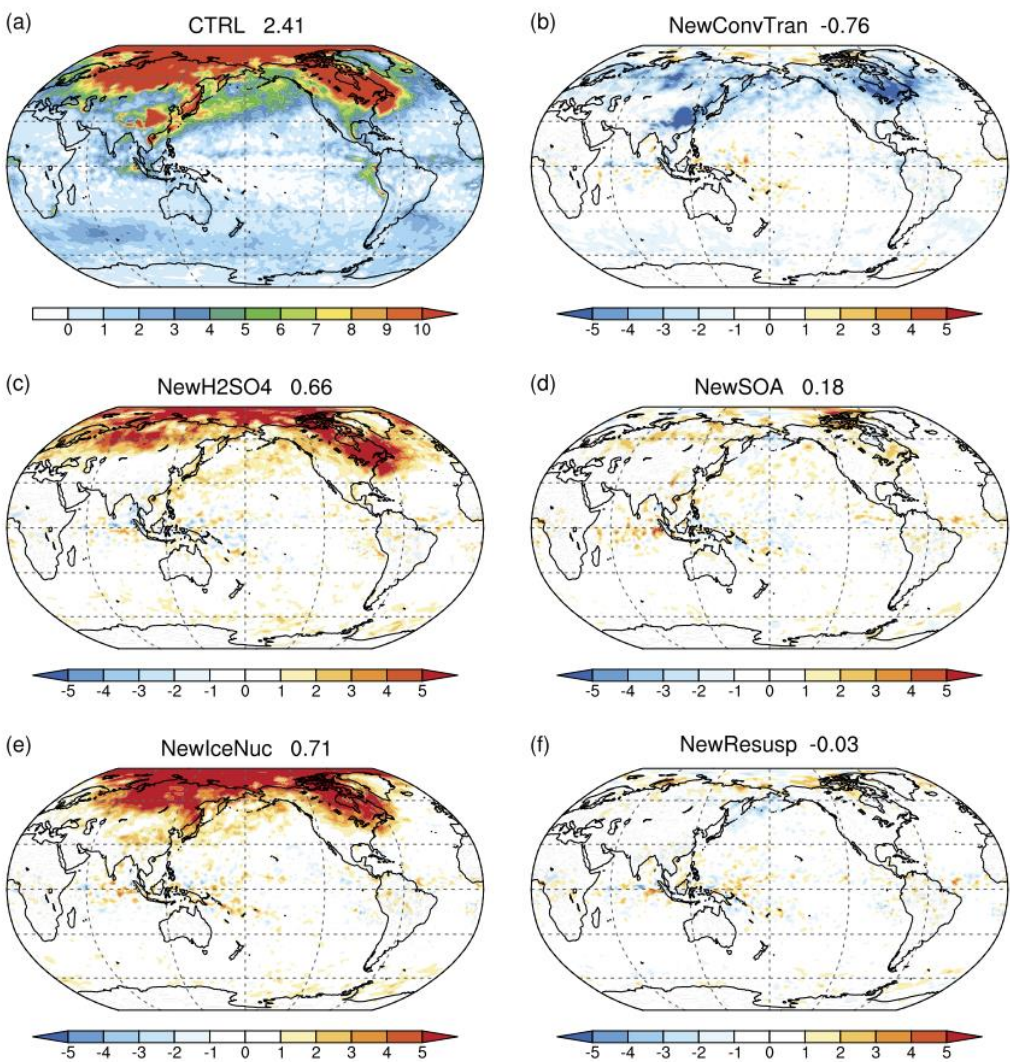


Figure 15: Same as Fig. 13 but for grid mean liquid water path (LWP).

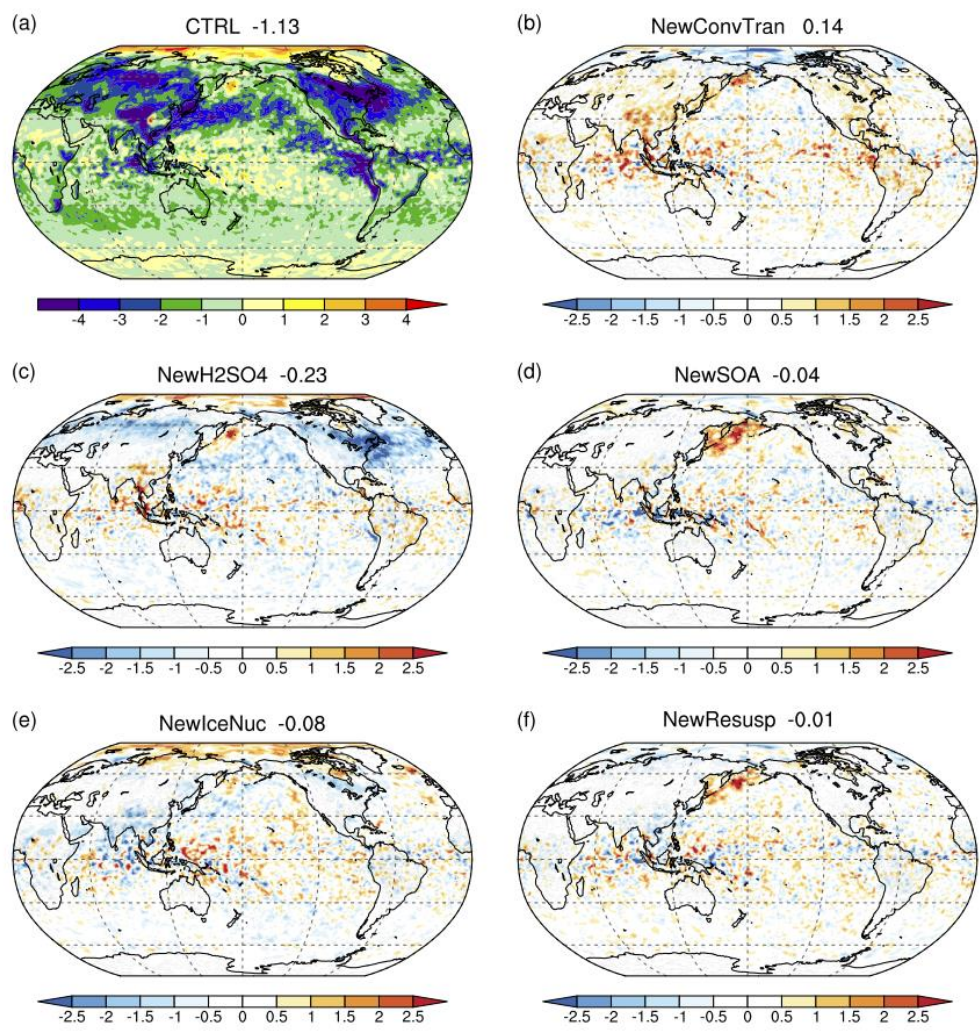


Fig. 16: Same as Fig. 13 but for net cloud forcing

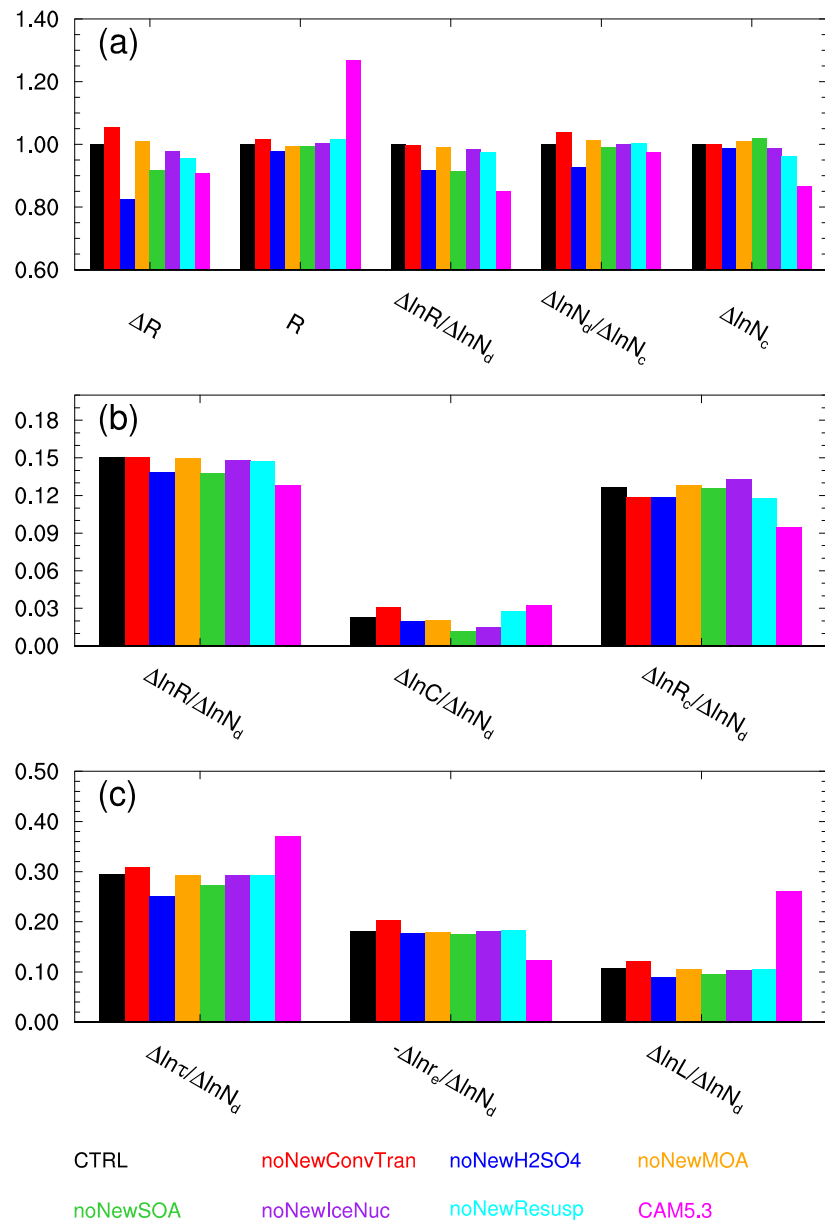


Figure 17: (a) Values of each term in the shortwave cloud forcing balance described in Eq. (1) for E3SMv1 PD/PI simulations (each of the other simulations has one new treatment excluded from the CTRL), compared to a CAM5.3 simulation from Ghan et al. (2016), normalized by CTRL; (b) Values of each term in Eq. (2) showing the contribution of relationship of warm cloud fraction C and in-cloud radiative forcing R_c with N_d to the susceptibility of R to N_d for all the simulations (globally averaged but not normalized). (c) Values of each term in Eq. (3) contributing to the relationship between cloud optical depth (τ) and N_d for warm clouds (globally averaged but not normalized).

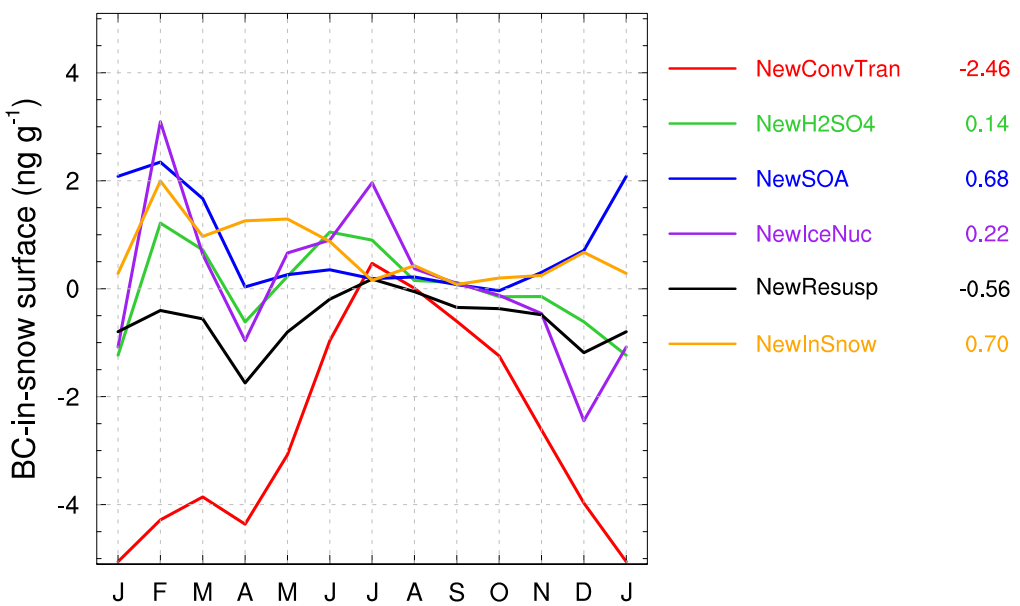


Figure 18: change in monthly mean BC-in-snow (surface layer) concentrations (defined as mass of BC contained by per unit mass of water with units of ng g^{-1}) due to the individual new treatment of aerosols in E3SMv1. It is calculated using the difference between CTRL and the corresponding sensitivity experiment (summarized in Table 1) with each new treatment excluded.

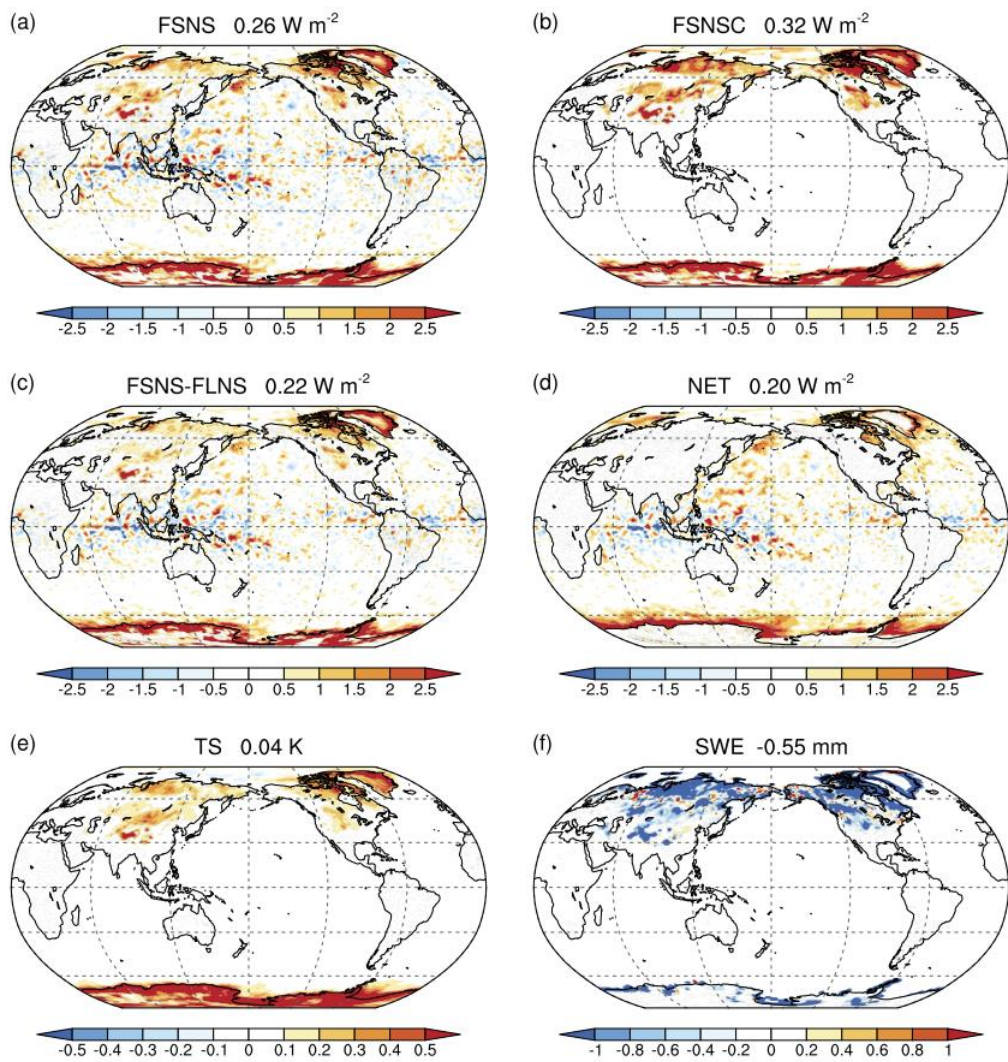


Figure 19: Impact of the new treatment related to BC and dust in snow (NewInSnow) on (a, b) SW radiative flux (W m^{-2}) at the surface under all sky and clear sky, respectively, (c) combined all-sky SW and LW fluxes at the surface, (d) net energy flux (combined radiative, sensible and latent heat fluxes), (e) surface temperature, TS (K), and (f) snow water equivalent (SWE, mm).

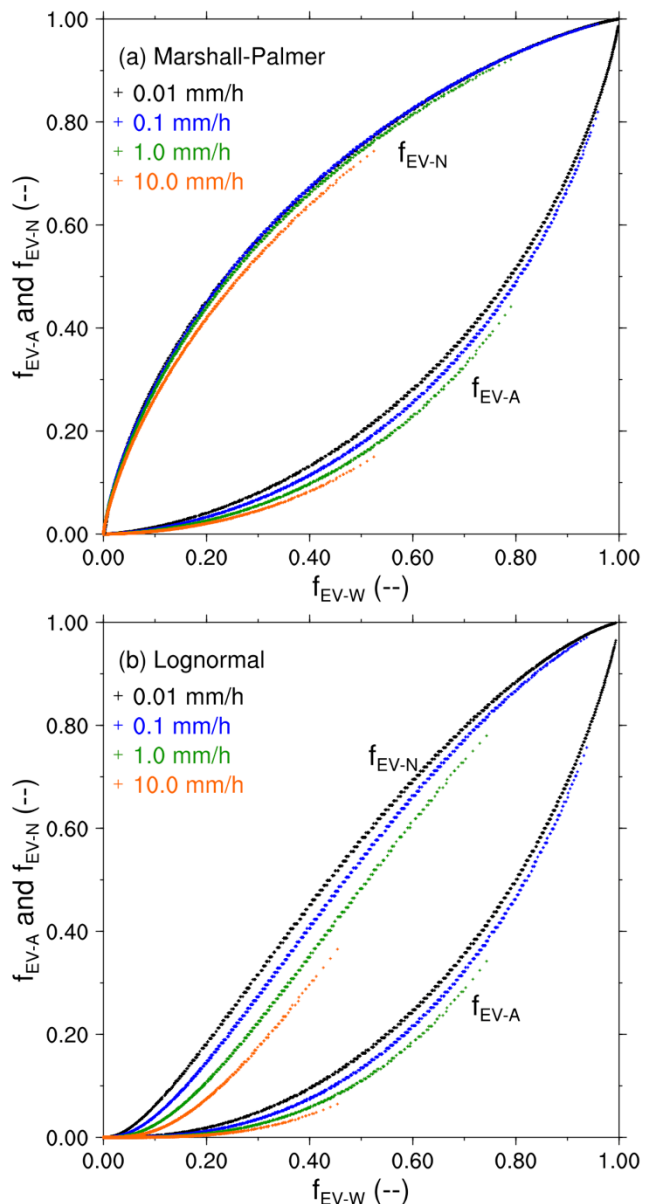


Figure A1. Evaporated fraction of precipitation-borne aerosol (f_{EV-A}) and (fully) evaporated fraction of raindrop number flux (f_{EV-N}) vs. evaporated fraction of precipitation water flux for (a) Marshall Palmer and (b) lognormal raindrop size distributions. Separate curves are for cloud-base rain rates of 0.01, 0.1, 1 and 10 mm h^{-1} . For each cloud-base rates, results cover a range of cloud-base heights and surface relative humidities, as described in text.

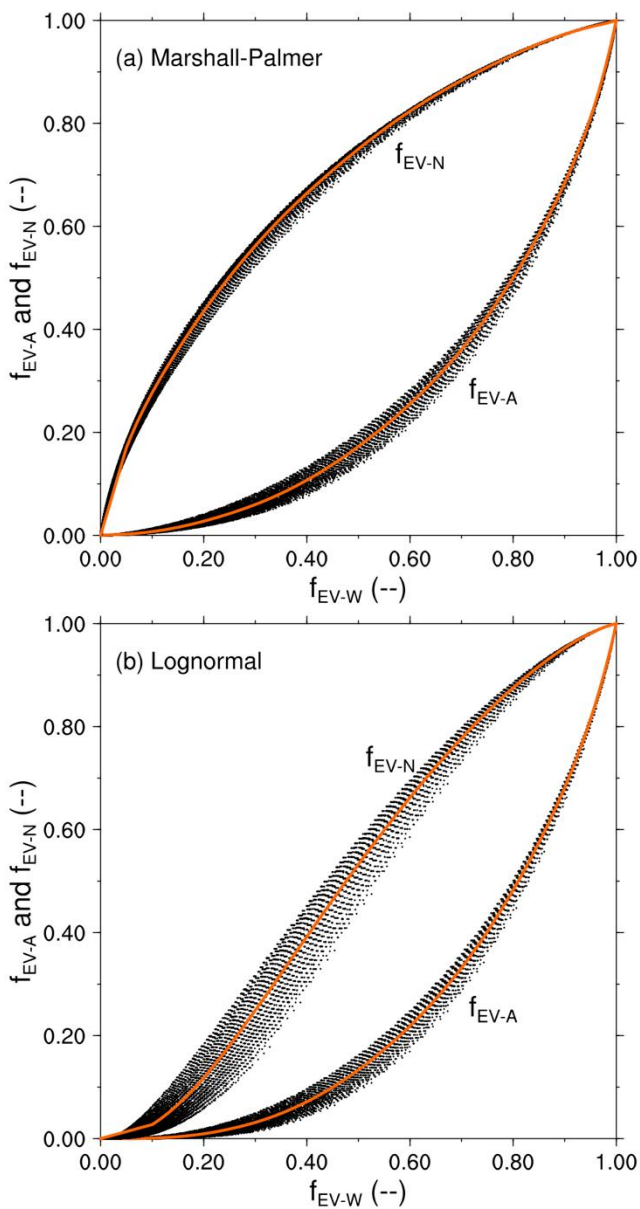


Figure A2. Evaporated fraction of precipitation-borne aerosol (f_{EV-A}) and (fully) evaporated fraction of raindrop number flux (f_{EV-N}) vs. evaporated fraction of precipitation water flux for (a) Marshall Palmer and (b) lognormal raindrop size distributions. Black dots are calculation results for the entire range of cloud-base rain rates, cloud-base heights, and surface relative humidities, as described in text. Red lines are 9th-order polynomial fits to the calculation results.